PART II

THEORETICAL ANALYSIS

CHAPTER TWO

FUNDAMENTAL CONCEPTS AND THEORETICAL BACKGROUND OF SPREAD-SPECTRUM SYSTEMS

2.1 INTRODUCTION

Spread-spectrum modulation was originally developed for military applications where resistance to jamming (interference) is of primary importance. However, there are civilian applications that may also benefit from the unique characteristics of spread-spectrum modulation. For example, it can be used to provide multipath rejection in a ground-based mobile radio environment. Another application is in multiple-access communication in which a number of independent users are required to share a common channel without an external synchronizing mechanism. Every user is allocated his own spreading code and coexists in a common spreading bandwidth with multiple other users. The unique properties of the spreading code make it possible to extract the transmitted data from the composite multi-user environment at the reference user's receiver. Thus, the system also provides a form of secure communication in a hostile environment such that the transmitted signal is not easily detected or recognized by unwanted listeners.

2.2 BASIC PRINCIPLES OF DSSS

In a DSSS communication system, [11], [12], [13], [14], the spectrum spreading is accomplished before transmission through the use of a spreading code that is independent of the data sequence. The same spreading code is used in the receiver (operating in synchronism with the transmitter) to despread the received signal so that the original data

may be recovered. The information-bearing signal is multiplied by a spreading code so that each information bit is divided into a number of small time increments. These small time increments are commonly referred to as chips. In this process the narrow bandwidth of the information-bearing signal is spread over a wide bandwidth with a factor L which equals the length of the spreading sequence. The two fundamental types of spread-spectrum systems are direct-sequence (DS) and frequency-hop (FH) spread-spectrum.

In order to classify as a spread-spectrum modulation technique, two criteria must be satisfied:

- The transmission bandwidth must be much larger than the information bandwidth.
- The resulting spread radio-frequency bandwidth must have no direct relation with the information signal bandwidth, i.e., it should be the result of a spreading process in which the spreading sequence or code is totally uncorrelated with the information signal.

Spread-spectrum communication techniques may be very useful in solving different communication problems. The amount of performance improvement that is achieved through the use of spread-spectrum, relative to an unspread system, is described in terms of a so-called processing gain (PG) factor. In spread-spectrum modulation an information-bearing signal is transformed into a transmission signal with a much larger bandwidth. The transformation is achieved by encoding (spreading) the information bearing signal with a spreading code signal that is independent of the data signal. This process spreads the power of the original data signal over a much broader bandwidth, resulting in a lower power spectral density than the unspread information signal. When the spectral density of the resultant SS signal starts to merge with or fall below the background noise level, the DSSS communication signal enters a state of low visibility or perception, making it hard to locate or intercept. This communication mode is commonly referred to as low probability of interception (LPI), and offers a form of security, which has previously been exploited for military applications, but are presently increasingly applied to a host of commercial applications. The PG of the spread-spectrum system can be defined as the ratio of transmission bandwidth to information bandwidth,

$$PG = \frac{B_T}{B_B} = \frac{T_b}{T_c} = \frac{R_c}{R_b} = L \tag{2.1}$$

where B_T is the transmission bandwidth, B_B the bandwidth of the information-bearing signal, T_b is one bit period of the data signal, T_c is one chip period of the spreading code, R_c

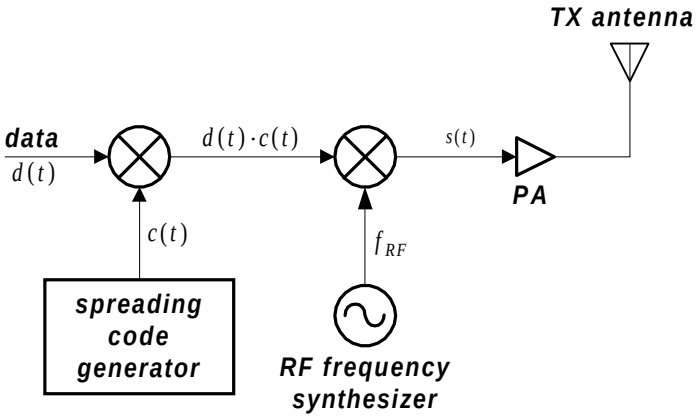

FIGURE 2.1: Conceptual block diagram of a DSSS transmitter

is the chip rate of the spreading sequence, R_b is the bit rate of the data signal and L is the length of the spreading code.

The receiver correlates the received signal with a synchronously generated replica of the spreading code signal to recover the original information-bearing signal. This implies that the receiver must know the spreading sequence or code used to spread or spread-spectrum modulate the data.

The basic spreading process in a direct sequence spread-spectrum system is illustrated in the conceptual block diagram of a DSSS transmitter in Figure 2.1. The information-bearing signal, $d(t)$, is multiplied by the spreading code, $c(t)$, and modulated onto a RF carrier frequency to obtain a final spread output signal, $s(t)$,

$$s(t) = d(t) \cdot c(t) \cdot \cos(2\pi f_{RF} t) \tag{2.2}$$

where f_{RF} is the RF carrier frequency.

The basic DSSS despreading process is shown in the conceptual block diagram of a DSSS receiver depicted in Figure 2.2. The incoming signal is received by the RF front-end, consisting of basically a noise reject bandpass filter, a LNA and a mixer to down-convert the RF signal to IF. This IF DSSS signal is despread and bandpass filtered, whereafter the despread signal is demodulated by means of a BPSK demodulator to recover the original information-bearing signal, $d(t)$. The relevant time domain signals of the spreading and despreading processes are displayed in Figure 2.3, while Figure 2.4 depicts the frequency spectra of these signals.

In the case of a high-power narrow-band interference or jamming signal, the interference

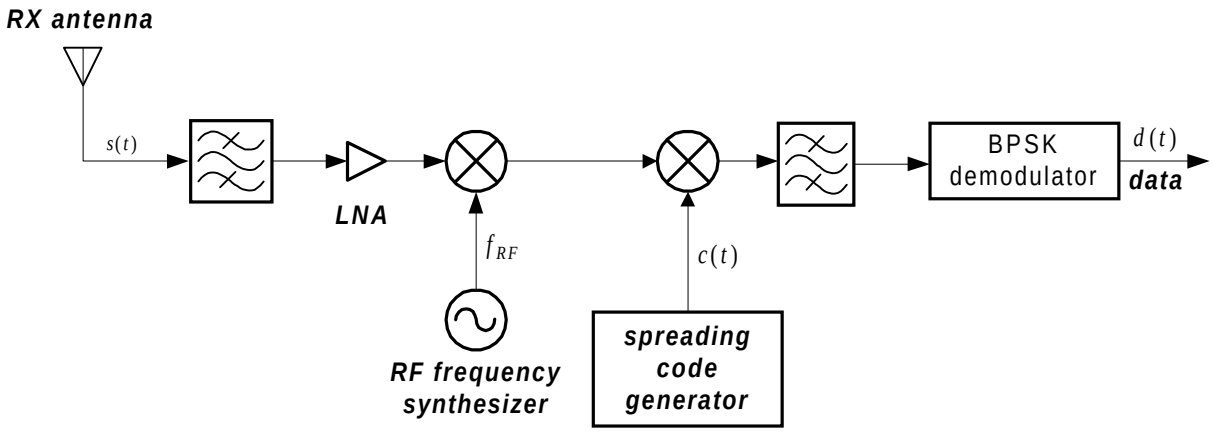

FIGURE 2.2: Conceptual block diagram of a DSSS receiver

or jamming signal is added to the spread data signal in the radio channel. In the despreading process at the receiver, the spread data signal is despread to its original narrow bandwidth and bandpass filtered to the double sideband information bandwidth, while the interference or jammer signal is spread by a factor equal to the spreading sequence length L, resulting in a low density wideband interference signal. Since only a portion of this low-density interference or jammer signal may fall within the actual information band after despreading, the interference power will be significantly reduced compared to the original full-power interference case.

Below are a number of alternative ways whereby spread-spectrum signals may be generated, namely:

- Direct-sequence spread-spectrum.
  The information-bearing signal is multiplied directly by a fast spreading code signal.

- Frequency hopping spread-spectrum.
  The carrier frequency at which the information-bearing signal is transmitted is rapidly changed according to the spreading code signal.

- Time hopping spread-spectrum.
  The information-bearing signal is not transmitted continuously. Instead the signal is transmitted in short bursts where the times of the bursts are decided by the spreading code signal.

- Chirp modulation.

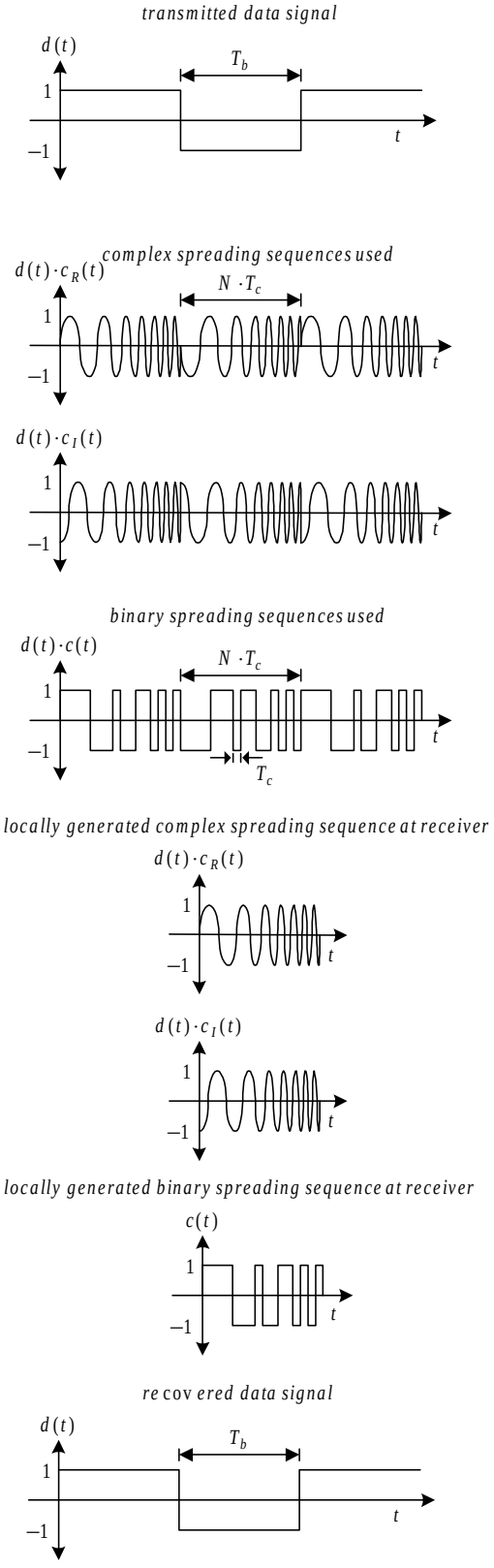

FIGURE 2.3: Signals in the time domain demonstrating the spreading-despreading process

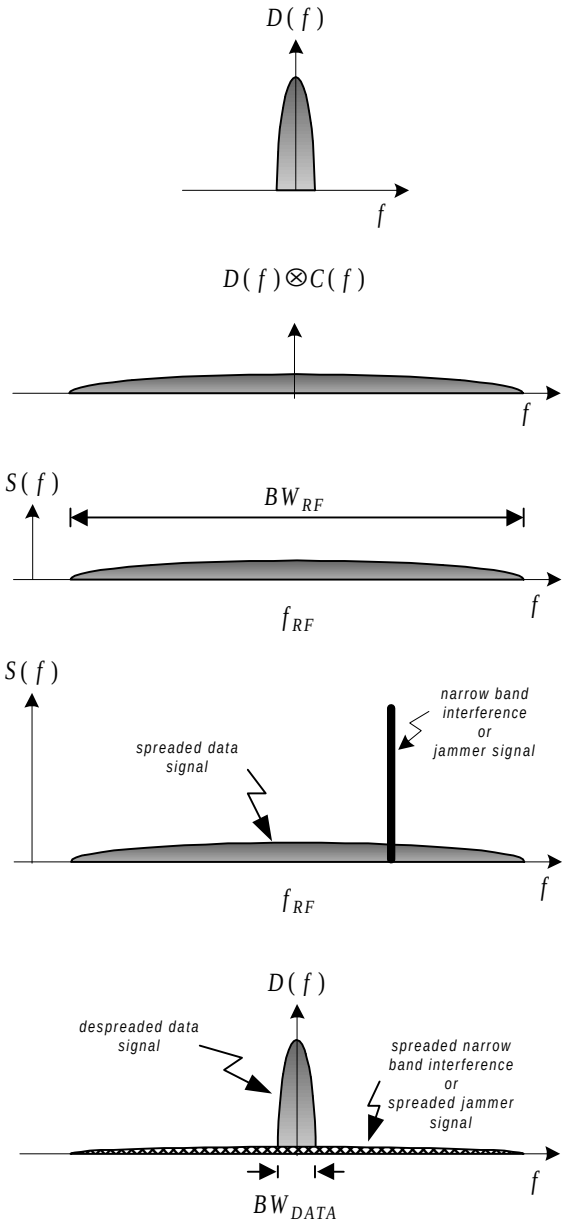

FIGURE 2.4: Signals in the frequency domain demonstrating the spreading-despreading process

This kind of spread-spectrum modulation is almost exclusively used in military radars. The radar continuously transmits a low power signal whose frequency is linearly varied (swept) over a wide range.

- Hybrid modulation.
  By combining two or more of the above mentioned spread-spectrum modulation techniques the advantages of both of the constituent techniques may be gained, and possible disadvantages may be overcome.

2.3 WHY SPREAD SPECTRUM ?

2.3.1 Advantages of DSSS

- Enhanced security and privacy in communications:
  The transmitted signal can only be despread and the data recovered if the spreading code is known to the receiver.

- Protection against multipath interference:
  In a radio channel there are more than one path between a transmitter and receiver. Due to reflections and refractions a signal will be received from a number of different paths. The signals of the different paths are all copies of the transmitted signal but with different amplitudes and phases. Adding these signals at the receiver will be constructive at some frequencies and destructive at others. In the time domain, this results in a dispersed signal. Spread-spectrum modulation combats this multipath interference and may in fact resolve it if the differential multipath delays are larger than the chip period. In such a case multipath diversity may be exploited by employing maximal ratio combining techniques such as provided by so-called RAKE receiver mechanisms.

- Low probability of intercept (LPI):
  Spread spectrum complicates the signal detection problem of a surveillance receiver by virtue of a larger frequency band to be monitored as well as a lower power spectral density of the signal to be detected in the spectrum-spreading process.

- Interference rejection and immunity:
  Cross-correlating the code signal with a narrowband signal will spread the power of the narrowband signal thereby reducing the interfering power in the information

bandwidth. This is illustrated in Figure 2.4, where it is assumed that narrowband interference is intensionally or non-intensionally added to the spread-spectrum signal during transmission. At the receiver the spread-spectrum signal is despread while the interference signal is spread, making it appear as background noise compared to the despread information signal. The overall effect is to gain a processing advantage for the DSSS-modulated information signal with respect to the narrowband interfering signal, making the DSSS signal more immune to interference.

- Low power density spectra:
  The power of the data information signal is spread over the total available spreading bandwidth of the DSSS communication system during the spreading process. This results in a much lower power spectral density compared to the corresponding narrowband modulation case, offering the advantage of low probability of detection and interception.

- High resolution ranging:
  In radar applications, ranging resolution is determined by the code rate (chip length) and code length (number of chips per code). The code repetition rate and length also determine the maximum unambiguous range. Ranging has been the most prominent and certainly the best known use of spread spectrum systems. Position location systems, such as for example the Global Positioning System (GPS), uses spread-spectrum principles to provide services such as vehicle location and tracking.

- Code division multiplexing for code division multiple access applications:
  If multiple users transmit a spread-spectrum signal at the same time in the same frequency band, the receiver will still be able to distinguish between the users provided each user has a unique spreading code with sufficiently low cross-correlation with other spreading codes. Correlating the received signal with a spreading code signal from a certain user will then only despread the signal of that user, while the other spread-spectrum signals will remain spread over a large bandwidth. Thus, within the information bandwidth, the power of the desired user will be much larger than the interfering power of the other users (interferers), provided that there are not too many simultaneous users, allowing the desired signal to be recovered (despread and extracted) with a minimum specified quality of service (QoS). It is exactly this interference rejection ability of a spread-spectrum system that facilitates multiple access services, i.e., co-existence of multiple users in the same communication band

and thus, efficient sharing of limited spectrum resources. For this reason, this synchronous form of spectrum sharing is often called spread-spectrum multiple-access (SSMA) or code-division multiple-access (CDMA), [15].

- Elimination of frequency planning in SS CDMA:
  The basic principle of cellular telecommunications is the ability to reuse available channel frequencies over a particular geographical area. In analog and TDMA-based systems every frequency cannot be reused in every cell, because such practice would cause unmanageable interference. The available frequencies must be utilised according to a well planned frequency reuse scheme over a number of cells and carefully coordinated to avoid interference with each other. In a CDMA system, all the users on a certain carrier share the same RF spectrum. The same RF carrier frequency is used in every cell site and in every sector of a sectorized cell site, resulting in a universal frequency reuse pattern. It is this unique universal frequency reuse strategy that gives CDMA its very large capacity increase over analog and TDMA-based technologies and eliminates the need for frequency planning.

- Improves spectral efficiency and capacity:
  CDMA provides larger spectral efficiency and system capacity than analog and TDMA-based systems, [16], by virtue of a larger channel/carrier reuse factor per coverage area. The universal frequency reuse strategy of CDMA has allowed mobile systems to achieve up to 20 times more capacity than first generation (1G) analog systems (FM/FDMA), and 4 to 6 times capacity increase over existing second generation (2G) digital TDMA or FDMA systems, [17].

- Voice activity detection:
  Voice activity detection , [15], is another variable which helps to increase the capacity of a CDMA system. CDMA takes advantage of voice activity gain through its use of variable rate vocoders. The principle behind the variable rate vocoder is to have it run at high speed, providing the best speech quality, only when voice activity is detected. When no voice activity is detected, the vocoder will drop its encoding rate. The variable rate vocoder uses up channel capacity only as needed. Since the level of interference created by all of the users directly determines system capacity, CDMA network capacity is maximized because the voice activity detection reduces the noise level in the system. In a typical phone conversation, a person is actively talking only about 35% of the time. The other 65% is spent listening to the other party, or is spent

in silence when neither party is speaking. This implies that system capacity could be increased by 65% using voice activity detection.

2.4 CAPACITY OF A CDMA SYSTEM

In a CDMA communication system, the capacity is interference limited, while it is bandwidth limited in FDMA and TDMA systems. Thus, the capacity of a CDMA system, [18], [17], [19], [13], [14], [11], will increase with a reduction of interference. As the number of users decrease, the interference level decreases and the link performance for each user increases. TDMA is a time-dimension-limited system in which there can be no additional users when all the time slots have been assigned. As the number of users increase, there is no interference caused by one mobile radio to the reception of another mobile radio at the cell cite. The number of users will increase until the number of time slots is exhausted. There after it is not possible to increase the number of users. Spread spectrum communication systems can tolerate some interference and the introduction of each additional active user raises the overall level of total interference to the base station receivers. The number of CDMA channels allowed in a star network depends on the total level of interference that can be tolerated by the CDMA system. Based on the fact that the CDMA system is limited by interference, spread spectrum CDMA systems place a greater premium on good overall mobile radio and system design than conventional narrowband FDMA and TDMA multiple-access radio systems.

Given the following assumptions for a digital cellular CDMA communication system:

- Power control is employed such that all uplink (mobile-to-base station) signals at the cell site are received with the same signal power level.
- All users are spread over the same total available bandwidth B_T.
- The interference between radios is modelled as Gaussian noise.
- Each user has a required bit error probability that defines a required E_b/N_o.
- A cell has a total number of M users.

For a single cell site with power control, all reverse link signals are received with the same power level. Thus composite uplink received signal at the base site will consist of the desired signal with power P_S and $M-1$ interfering users, each also of power P_S. The signal-to-noise (interference) power ratio can be written as

$$SNR = \frac{P_S}{(M-1)P_S} = \frac{1}{M-1} \tag{2.3}$$

The bit energy-to-noise density ratio is obtained by dividing the signal power P_S by the information bit rate, R_b, and dividing the noise (interference) by the total spreading bandwidth or transmission bandwidth, B_T. Thus the bit energy-to-noise density ratio is

$$E_b/N_o = \frac{P_S/R_b}{(M-1)P_S/B_T} = \frac{B_T/R_b}{M-1} = \frac{PG}{M-1} \tag{2.4}$$

By solving 2.4 for M, the capacity of the cell in terms of channels/transmission bandwidth B_T is found, given by

$$M = 1 + \frac{PG}{E_b/N_o} \cong \frac{PG}{E_b/N_o} \tag{2.5}$$

for M large, and with the assumption that each interferer is transmitting continuously.

The required E_b/No depends on how much error correction coding is used and how well the radio is designed, for a given bit error probability. According to Shannon's limit in AWGN, error free communication is possible for

$$E_b/N_o = ln2 = 0.69 = -1.59dB \tag{2.6}$$

and thus for this Shannon limit

$$M = 1.44 \times PG. \tag{2.7}$$

Spread spectrum systems can have more users per cell than traditional systems, which are limited by the number of dimensions, such as available frequency bands (FDMA) or time slots (TDMA). With practical CDMA systems, it may be difficult to accommodate this many users in a single cell, but TDMA and FDMA systems, however, use only up to 20 percent of this theoretical capacity to ensure the practical isolation between non-interfering channels.

The interference at the base station will come from both within a cell, as well as from outside the cell. The interference coming from outside the cell can be accounted for by a factor f, and then Equation 2.5 becomes

$$M = \frac{PG}{E_b/N_o} f \tag{2.8}$$

The capacity of a CDMA system can be extended by lowering the level of interference. There are several methods of decreasing the interference level in a CDMA communication system, i.e., voice activity and data applications, [20], antenna sectorisation, frequency reuse, power control and multibeam antennas.

CHAPTER THREE

COMPLEX SPREADING SEQUENCES

3.1 INTRODUCTION

In a CDMA system the capacity is limited by the amount of MUI present. Every user in the CDMA system uses it's own unique spreading sequence. At the receiver the user performs a correlation between the received signal and his spreading sequence, stored or generated at the receiver. The received signal consists of the sum of the spreading sequence of the reference user and the spreading sequences of all other users. During the despreading process in the receiver, both an **A**uto-**C**orrelation (AC) and a **C**ross-**C**orrelation (CC) function are performed. The value of the CC is not necessarily zero and therefore the spreading sequences of the other users generate noise in the process of signal detection. This noise is known as multi-user-interference (MUI) and is directly proportional to the number of users in the CDMA system.

Thus, the spreading sequences used in a CDMA system must have certain correlation properties to ensure a large capacity and high performance of the system. Two of the most important properties of spreading sequences are their AC and CC characteristics. The AC function must have a high peak at zero-shift, while the off-peak values of the AC and all the values of the CC functions have to be very small. For the ideal case these off-peak AC values and the CC values must be zero. These properties are summarized in equation 7.5.16, p733 in [21], and will be used to evaluate the sequences described below.

In [22] a complete performance analysis of direct sequence spread-spectrum multiple-access (DS/SSMA) communications with deterministic complex (non-binary and polyphase) signature sequences has been done. The probability of bit error (PBE)

performance of different types of complex sequences is compared to that of Gold sequences. In the calculation of the PBE the computational upper and lower bounding technique and the Gaussian approximation method have been used. The general outcome of the analysis was that both the correlation characteristics and the performance of the complex spreading sequences are better than that of binary Gold sequences.

The maximum value of the out-of-phase periodic auto correlation and periodic cross correlation C_{max} functions has been derived by [23] and [24] for families of spreading sequences of size M, sequence length L, and is given by

$$C_{max} = \begin{cases} \sqrt{2(L+1)}+1, & Goldsequences, L = 2^r - 1, rodd \\ \sqrt{L+\sqrt{2(L+1)}+2}, & nearoptimal4\phi sequences, L = 2^r - 1, rodd \\ \sqrt{L}, & FZCsequences, Loddprime \end{cases} \quad (3.1)$$

Zadoff-Chu complex spreading sequences have the best possible periodic correlations when the sequence length L is an odd prime.

3.2 SPREADING CODES

The complex spreading sequences used in this dissertation are derived from the family of **Z**adoff-**C**hu (ZC) sequences [9], which is a sub-class of the **G**eneral-**C**hirp-**L**ike (GCL) sequences. The rth ZC sequence is defined by

$$a(r,k) = \begin{cases} W_L^{\frac{k^2}{2}+qk} & ; Leven \\ W_L^{\frac{k(k+1)}{2}+qk} & ; Lodd \end{cases} \quad (3.2)$$

here W_L denotes a complex Lth root-of-unity, defined as

$$W_L = e^{-j\frac{2\pi r}{L}} \quad (3.3)$$

where $j = \sqrt{-1}$, r is any integer relatively prime to L, $k = 0, 1, 2, \ldots, L-1$, denoting the primary values of the sequence, and q is any integer. The family size equals $N = m - 1$ of length $L = m^2$. The real and imaginary parts of a typically eight times over-sampled sequence, with $r = 1$ and $L = 121$, is illustrated in Figure 3.1.

For an odd value of m, the unfiltered sequence exhibit perfect periodic CC properties, i.e., the peak AC values and the peak secondary AC values fall below the so-called Welch bound, which is commonly used as a figure of merit in the evaluation of correlation properties of families of spreading sequences.

To prevent spectral overlap in a communication system it is necessary to filter these spreading sequences. The filtering process must be chosen in such a way that the correlation characteristics of the spreading signal are not adversely affected. The ZC sequences consist only of the samples generated by Equation 3.2 and the values interpolated by the filtering process do not form part of the spreading sequence. Thus, the absolute phase difference between successive samples is not very important and any values can be chosen as interpolation values, as long as the primary values of the original ZC sequence do not change. The value of the absolute phase difference between successive samples can be reduced modulo π, and the resulting phase difference can then be linearly interpolated on the unit circle. All the samples are taken from the unit circle and the filtered sequence thus have a constant envelope. This filtering technique is described in detail in [25].

The double sided bandwidth of the filtered ZC spreading sequence, for all the possible values of r, can be calculated as

$$BW = \frac{f_{sample}}{samples\ per\ chip}\ [Hz] \tag{3.4}$$

The real and imaginary parts of the root-of-unity filtered complex spreading sequence 1 and 6 of length, $L = 121$, and samples per chip, $spc = 8$, are depicted in Figures 3.1 and 3.4, while the real vs. imaginary parts of sequence 1 and 6 are shown in Figures 3.2 and 3.5, respectively. The power spectral densities (PSD) for sequence 1 and sequence 6 are shown in Figures 3.3 and 3.6, respectively.

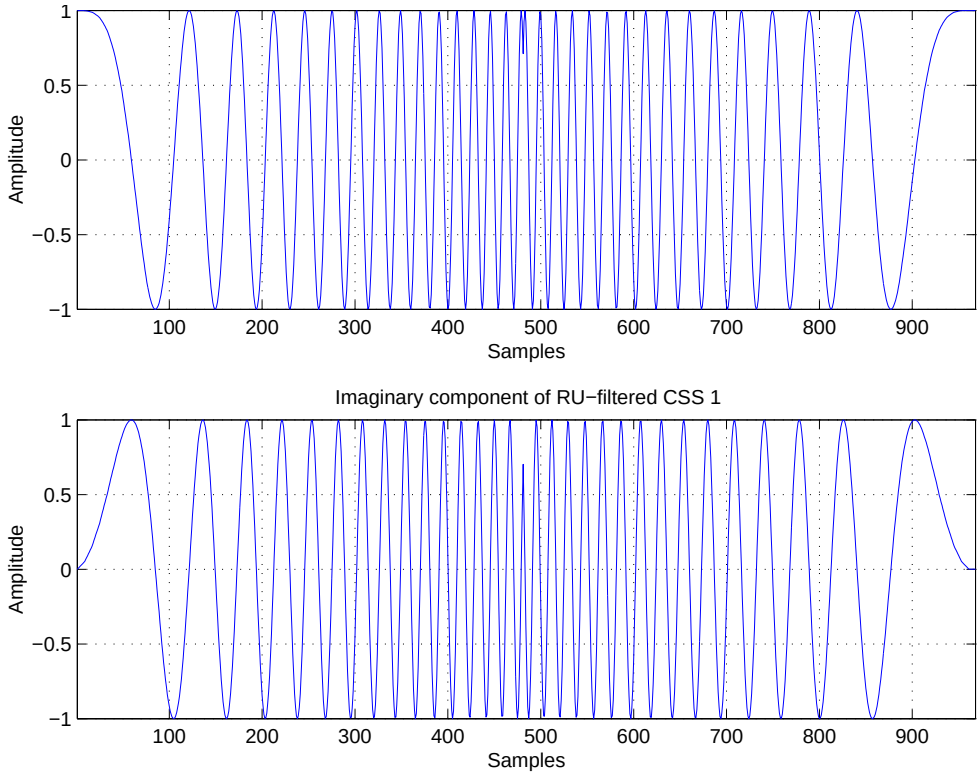

FIGURE 3.1: The Real, (a), and Imaginary, (b), part of complex spreading sequence 1. $(L = 121, RU\,filtered, spc = 8)$

3.2.1 Correlation Bounds

Sets of periodic sequences with good correlation properties are required for a variety of engineering applications, and much effort has been spent on design techniques for such sequences. It can be observed generally that if the set of sequences has good AC properties, then the CC properties are not very good. On the other hand, if the set of sequences has good CC properties, then the AC properties are not very good. A compromise has therefore to be made between the AC and CC properties of a particular family of spreading sequences for a specific application.

There is considerable literature on singular signals with good AC function, but little on sets of signals with good CC [26]. A lower bound to the maximum CC value for a family of complex spreading sequences was first derived by Welch [26]. Around the same time, Sidelnikov [27] derived a lower bound on the maximum value of CC of such sequences. Both Welch and Sidelnikov bounds have since been used extensively in the design and analysis of sequences for CDMA [26], [28], [29], [30], [31] and [32]. The criteria for DS-SSMA signal design are the minimization of the absolute value of the periodic and aperiodic cross-correlation (CC) between the signals. This criteria for sequence selection

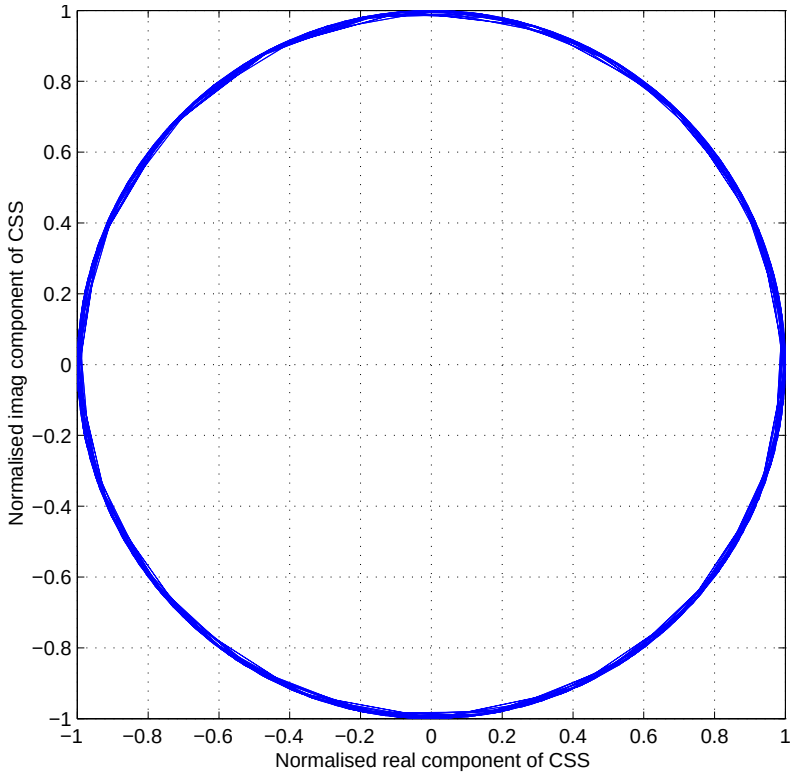

FIGURE 3.2: Real vs. Imaginary part of complex spreading sequence 1. $(L = 121, RU filtered, spc = 8)$

may not correspond to any DS-SSMA network performance measure, but it can be argued that a signal set which optimizes the network performance has to have small periodic and aperiodic CC values for all relative sequence shifts. The rule is to find good signals among the signal sets with small values of periodic and aperiodic CC.

The Welch's and Sidelnikov's lower bounds have been used as a benchmark for testing the merit of complex valued sequences. In general Welch's bound applies to complex vectors in general with no constraints on their sequence elements, whereas Sidelnikov's bound applies only to complex root of unity sequences with constant envelope [33].

3.2.1.1 The Welch Bound

The Welch bound [26] (normalised with respect to L) for the periodic case is defined as

$$\theta_{p(max)} \geq \sqrt{\frac{N-1}{L \cdot N - 1}} \tag{3.5}$$

It can be seen that for large L and a fixed value of N, Equation 3.5, becomes

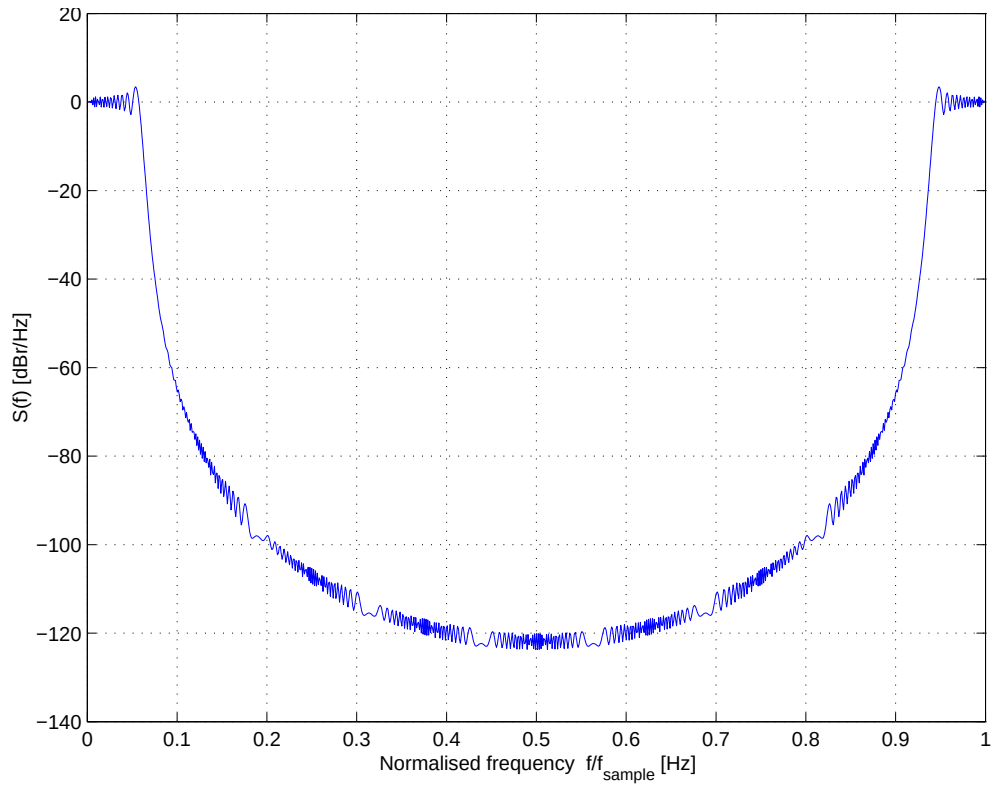

FIGURE 3.3: Power spectral density (PSD) of complex spreading sequence 1. $(L = 121, RU filtered, spc = 8)$

$$\theta_{p(max)} = \frac{1}{\sqrt{L}} \tag{3.6}$$

whereas the aperiodic case (normalised with respect to L) is given as

$$\theta_{a(max)} \geq \sqrt{\frac{N-1}{N(2L-1)-1}} \tag{3.7}$$

where N and L denote family size and sequence length, respectively.

3.2.1.2 The Sidelnikov Bound

The Sidelnikov bound (normalised with respect to L) states that for any $N \geq L$

$$\theta_{p(max)} > \frac{\sqrt{2 \cdot L - 2}}{L} \tag{3.8}$$

According to [31], Welch's bound is tighter than Sidelnikov's bound by the factor of $\sqrt{2}$, for large family sizes N. In recent years several researchers have tried to improve on the Welch's and Sidelnikov's bounds [30] and [32]. Since large family sizes are needed for CDMA applications, the work reported is mainly concentrated on improving Welch's and

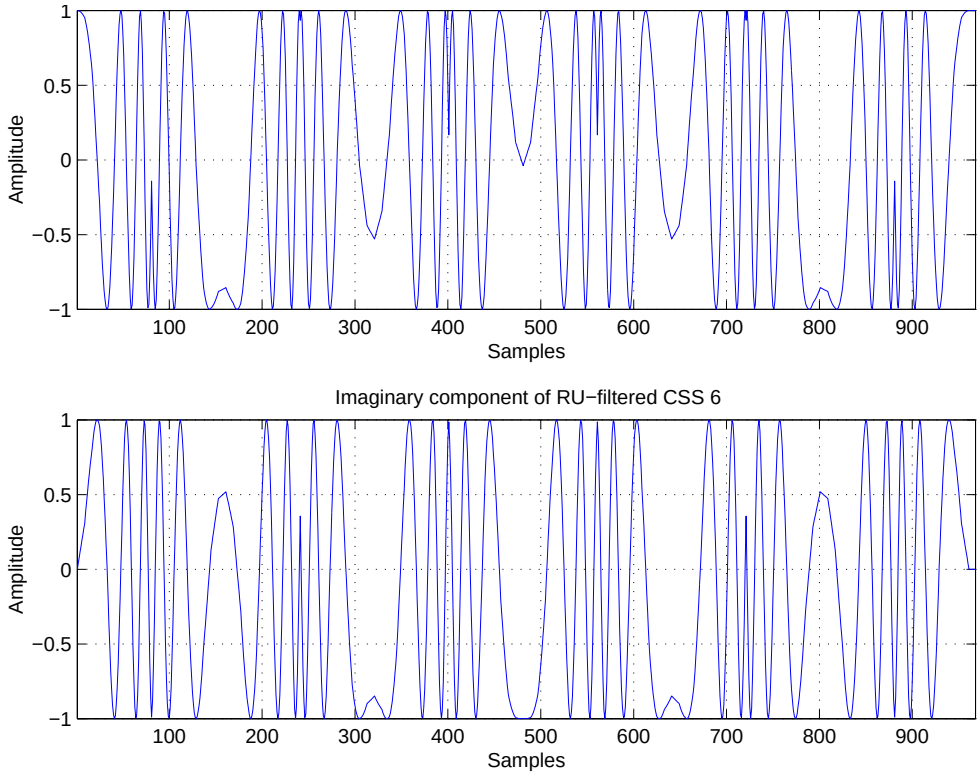

FIGURE 3.4: The Real, (a), and Imaginary, (b), part of complex spreading sequence 6. $(L = 121, RU filtered, spc = 8)$

Sidelnikov's bound for the case when N is larger than L. It is not possible to achieve N greater than L for the complex GCL sequences under consideration, with the exception of Quadri-phase sequences. Therefore, the comparison will be made on the basis of Welch's bound, which is usually treated as a lower bound on the maximum correlation values., i.e., it is considered to be a fundamental bound on the sum of the squares of the magnitudes of the inner products between the codes.

The bounds described above do not allow the design of correlation value and N independently. They rather dictate the limits within which all the code designs must lie. Since the design margin is very restrictive, the implication of these bounds for CDMA system designers is that it might be difficult to achieve new families of spreading sequences with large family sizes with good correlation properties [33].

In [23], it has been shown that the maximum magnitude of the periodic auto correlation (PAC) and periodic cross correlation (PCC) functions are related through an inequality, providing the lower bound on the maxima if the value of the other is specified.

$$\left\{\frac{\theta_c^2}{L}\right\} + \frac{L-1}{L(N-1)} \cdot \left\{\frac{\theta_a^2}{L}\right\} \geq 1 \tag{3.9}$$

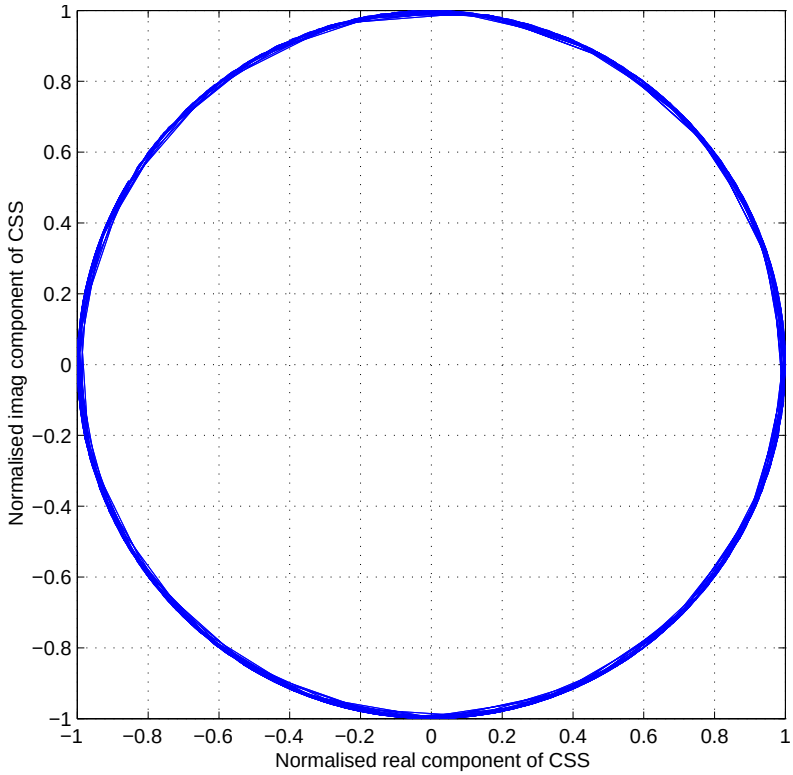

FIGURE 3.5: Real vs. Imaginary part of complex spreading sequence 6. $(L = 121, RU filtered, spc = 8)$

where L is the sequence length, N the family size, θ_a the maximum periodic AC peak and θ_c the maximum periodic CC peak.

When we substitute the maximum magnitude of the PAC, i.e., $\theta_a = 0$ in Equation 3.9, the lower bound for the maximum magnitude of the PCC is given by $\frac{1}{\sqrt{L}}$, which corresponds to Welch's bound, i.e., Equation 3.6.

Similarly maximum AAC and ACC function magnitudes are related through an inequality providing the lower bound on the maxima if the value of the other is specified

$$\frac{2L-1}{L}\left(\frac{C_c^2}{L}\right) + \frac{2(L-1)}{L(N-1)} \cdot \left(\frac{C_a^2}{L}\right) \geq 1 \tag{3.10}$$

where L again denotes the sequence length and N the family size, C_a the maximum secondary aperiodic AC peak and C_c the maximum aperiodic CC peak.

It has been shown in [23] that the lower bound on C_c, if C_a is given, is

$$\frac{C_{max}^2}{L^2} = max\left\{\frac{C_a^2}{L^2}, \frac{C_c^2}{L^2}\right\} \geq \frac{N-1}{2LN-N-1} \tag{3.11}$$

which is a result due to Welch [26], i.e., Equation 3.7.

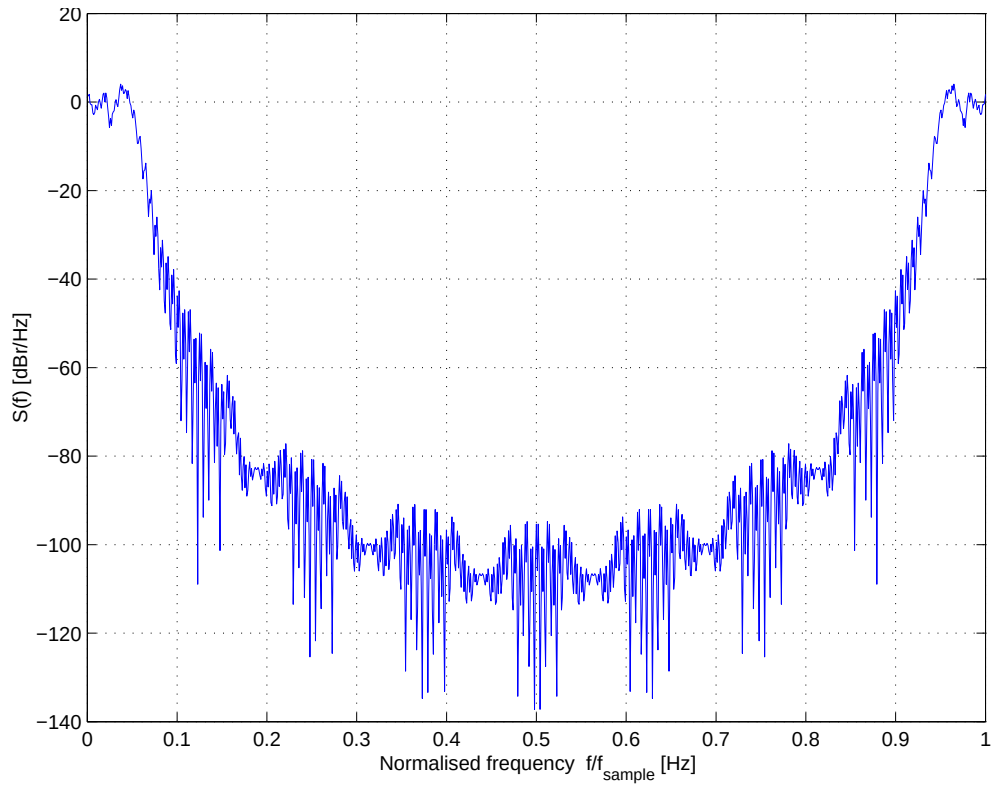

FIGURE 3.6: Power spectral density (PSD) of complex spreading sequence 6. $(L = 121, RU filtered, spc = 8)$

3.2.2 Autocorrelation Function

The sequence $\{s_k\}$ of length L has periodic AC function, $R_{ss}[l]$, given as

$$R_{ss}[l] = \sum_{k=0}^{L-1} s[k] \cdot s^*[k+l]_{mod\,L} \tag{3.12}$$

where * denotes the complex conjugate, the index $[k+l]$ is computed modulo L, and the time shift is l.

Thus for the ZC sequences, the periodic AC function is

$$R_{ss}[l] = \sum_{k=0}^{L-1} W_L^{\frac{k(k+1)}{2}} \cdot W_L^{\frac{-(k+l)_{mod\,L}\,((k+l)_{mod\,L}+1)}{2}} \tag{3.13}$$

for $q = 0$ and L odd.

The periodic AC functions for the ZC sequences 1 and 6, for a length of 121, can be seen in Figures 3.7, 3.8 and Figures 3.9, 3.10, respectively.

For a sequence s_k of length L the aperiodic AC function is defined as

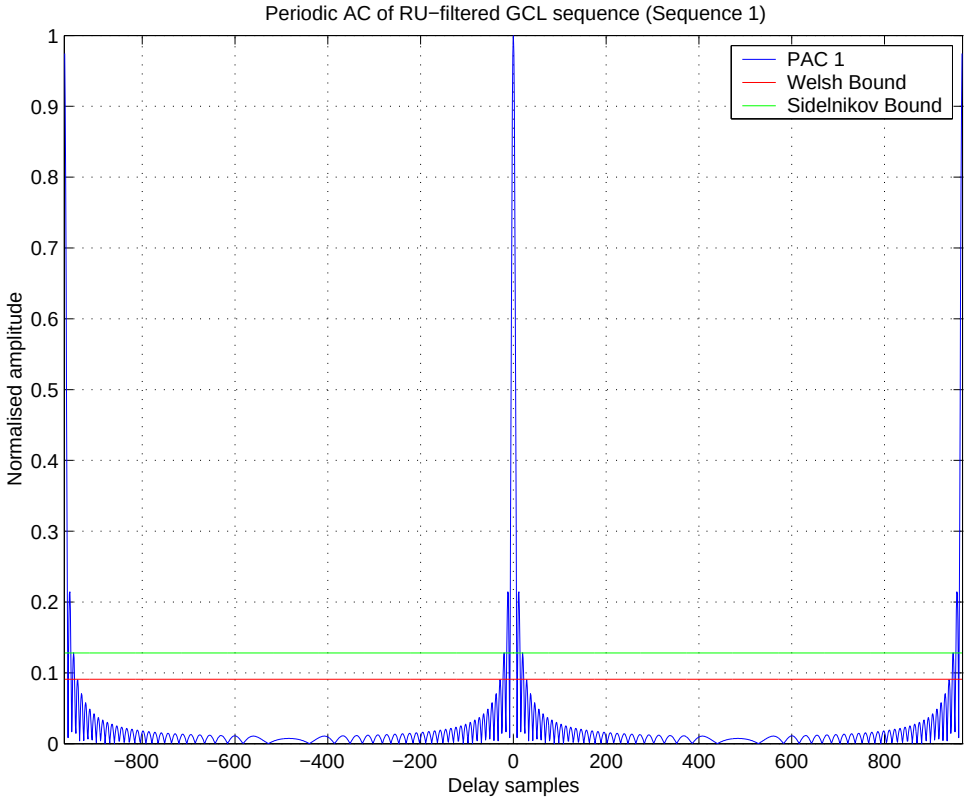

FIGURE 3.7: Periodic Auto Correlation (PAC) function of complex spreading sequence 1. $(L = 121, RUfiltered, spc = 8)$

$$R_{ss}[l] = \int_{-\infty}^{\infty} s[l] \cdot s^*[t+l]\, dl \tag{3.14}$$

where * denotes the complex conjugate and the time shift is l.

In discrete time notation the aperiodic AC function can be expressed as

$$R_{ss}[l] = \begin{cases} \sum_{k=0}^{L-1-l} s[l] \cdot s^*[k+l] & ;0 \leq l \leq L-1 \\ \sum_{k=0}^{L-1+l} s[k-l] \cdot s^*[k] & ;1-L \leq l < 0 \\ 0 & ;\mid l \mid \geq L \end{cases} \tag{3.15}$$

For ZC sequences the aperiodic AC function is

$$R_{aa}[l] = \begin{cases} \sum_{k=0}^{L-1-l} W_L^{\frac{k(k+1)}{2}} \cdot W_L^{\frac{-(k+1)(k+l+1)}{2}} & ;0 \leq l \leq L-1 \\ \sum_{k=0}^{L-1+l} W_L^{\frac{(k-l)(k-l+1)}{2}} \cdot W_L^{\frac{-k(k+l)}{2}} & ;1-L \leq l < 0 \\ 0 & ;\mid l \mid \geq L \end{cases} \tag{3.16}$$

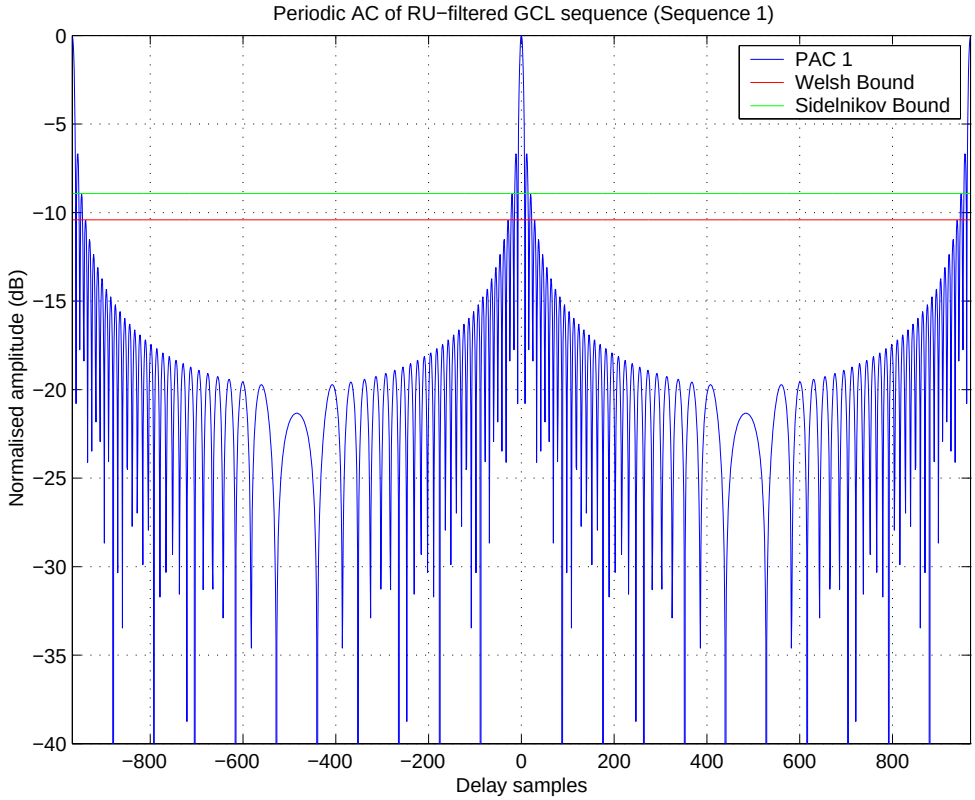

FIGURE 3.8: Periodic Auto Correlation (PAC) function of complex spreading sequence 1 in decibels. $(L = 121, RU filtered, spc = 8)$

for $q = 0$ and L odd.

The aperiodic AC functions for the ZC sequences 1 and 6, for a length of 121, can be seen in Figures 3.11, 3.12 and Figures 3.13, 3.14, respectively.

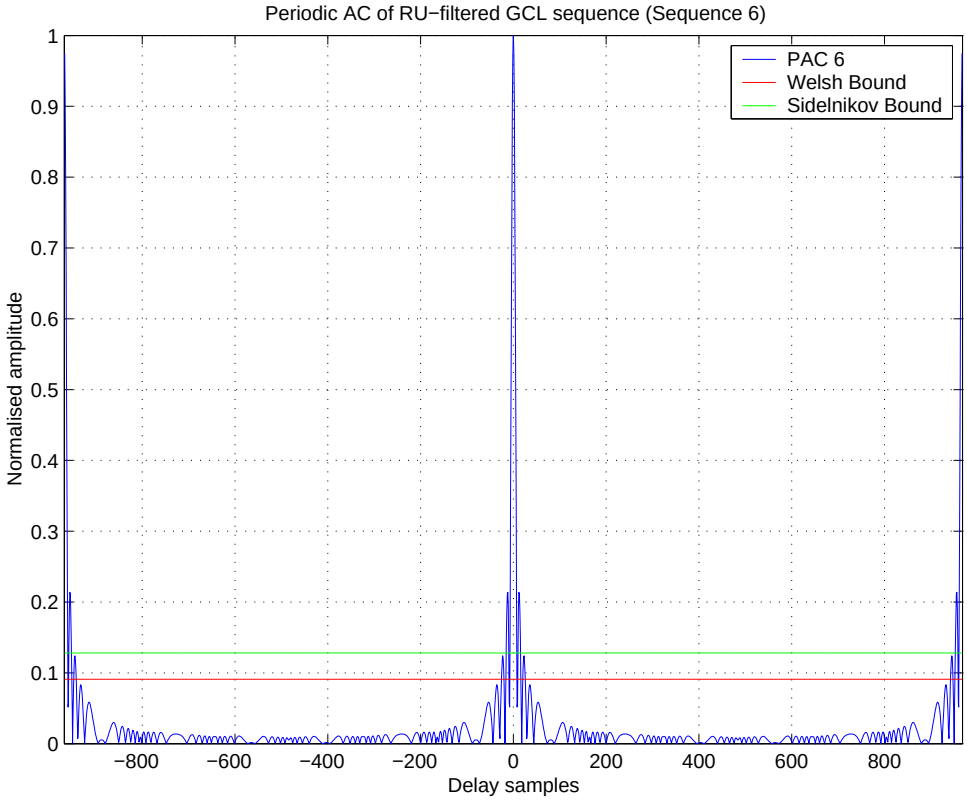

FIGURE 3.9: Periodic Auto Correlation (PAC) function of complex spreading sequence 6. $(L = 121, RUfiltered, spc = 8)$

3.2.3 Cross Correlation Function

The CC function shows the correspondence between two signals at different time shifts. The periodic CC function between any two sequences s_k and u_k, both of length L, is defined as

$$R_{su}[l] = \sum_{k=0}^{L-1} s[k] \cdot u^*[(k+l)_{modL}] \tag{3.17}$$

where $*$ denotes the complex conjugate, the index $(k + l)$ is computed modulo L, and the time shift is l.

Thus for the ZC sequence the periodic CC function is

$$R_{ab}[l] = \sum_{k=0}^{L-1} W_{L_a}^{\frac{k(k+1)}{2}} \cdot W_{L_a}^{\frac{-(k+l)_{modL}((k+l)_{modL}+1)}{2}} \tag{3.18}$$

for $q = 0$ and L odd.

The periodic cross correlation functions between spreading code number 1 and 6 are shown in Figures 3.15 and 3.16.

The aperiodic CC function between any two sequences s_k and u_k, both of length L, in discrete time notation is defined as

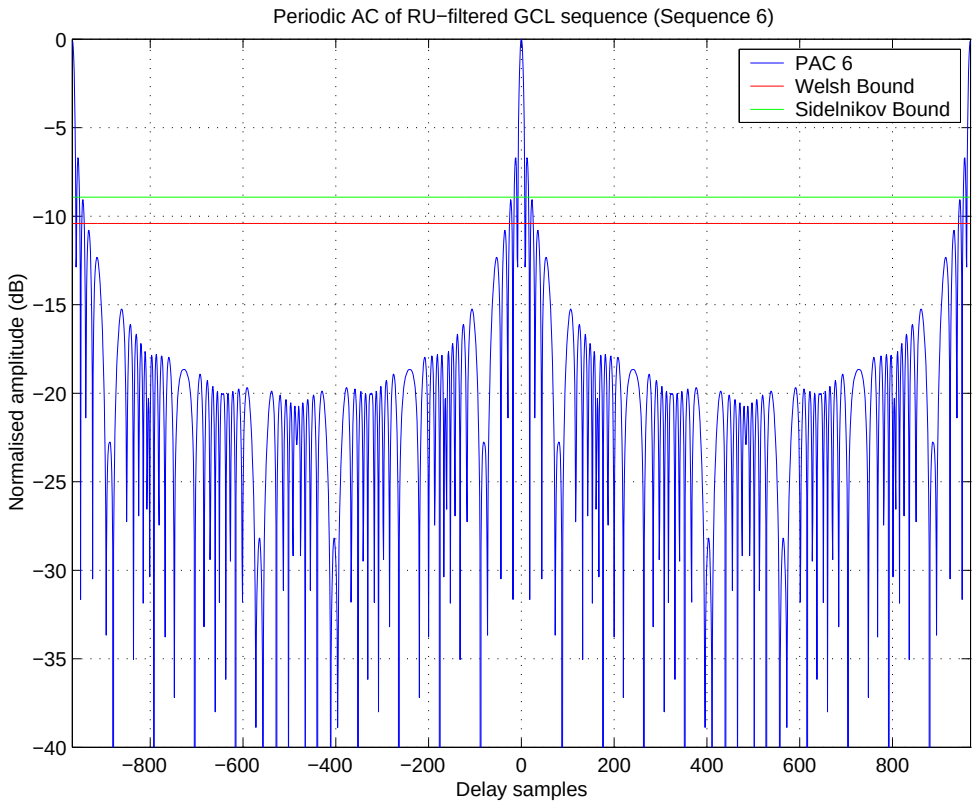

FIGURE 3.10: Periodic Auto Correlation (PAC) function of complex spreading sequence 6 in decibels. $(L = 121, RU\,filtered, spc = 8)$

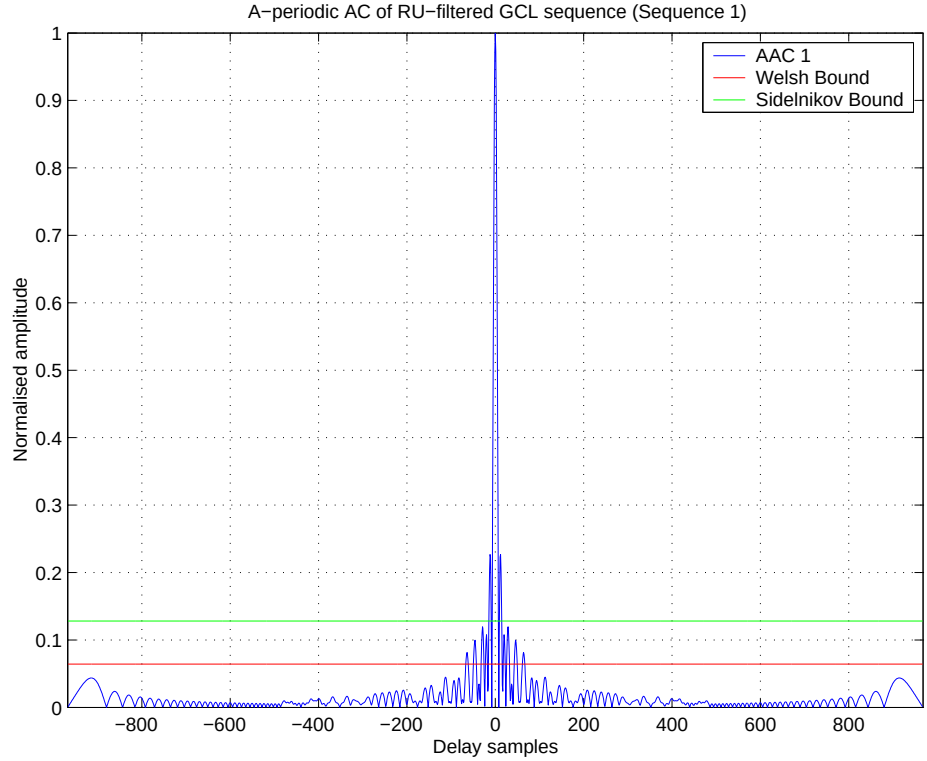

FIGURE 3.11: Aperiodic Auto Correlation (AAC) function of complex spreading sequence 1. $(L = 121, RU\,filtered, spc = 8)$

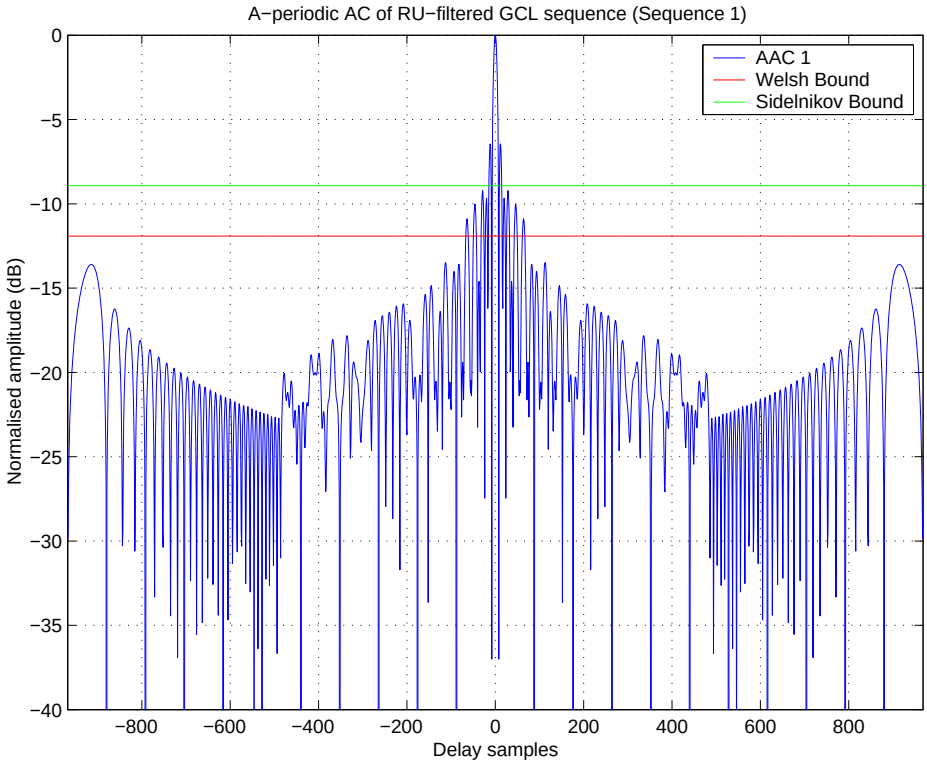

FIGURE 3.12: Aperiodic Auto Correlation (AAC) function of complex spreading sequence 1 in decibels. $(L = 121, RU filtered, spc = 8)$

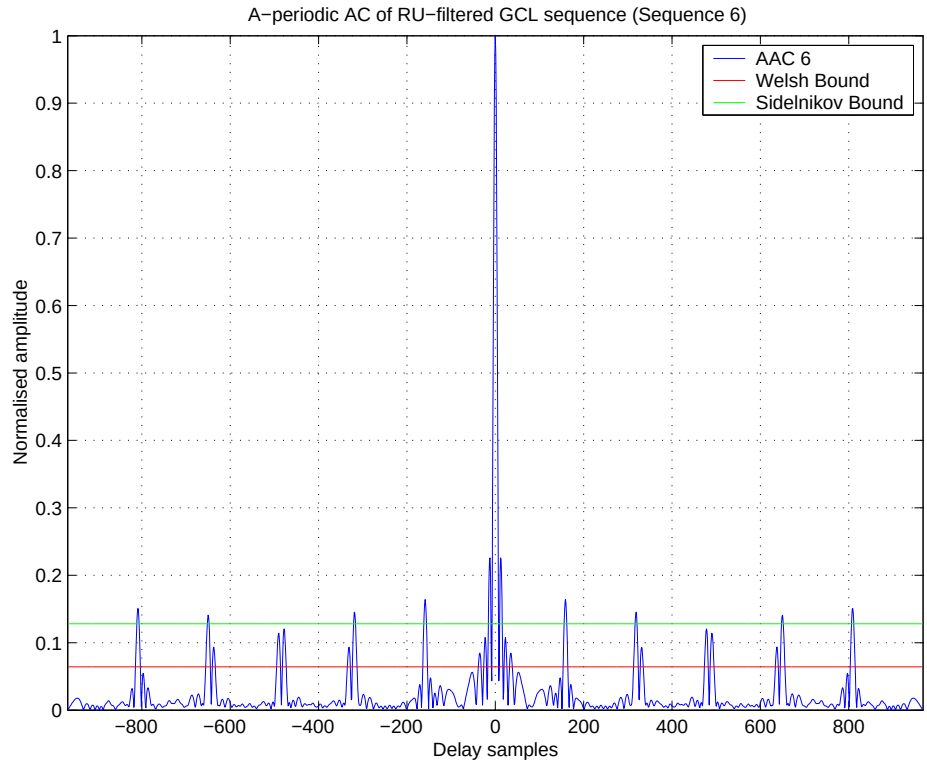

FIGURE 3.13: Aperiodic Auto Correlation (AAC) function of complex spreading sequence 6. $(L = 121, RU filtered, spc = 8)$

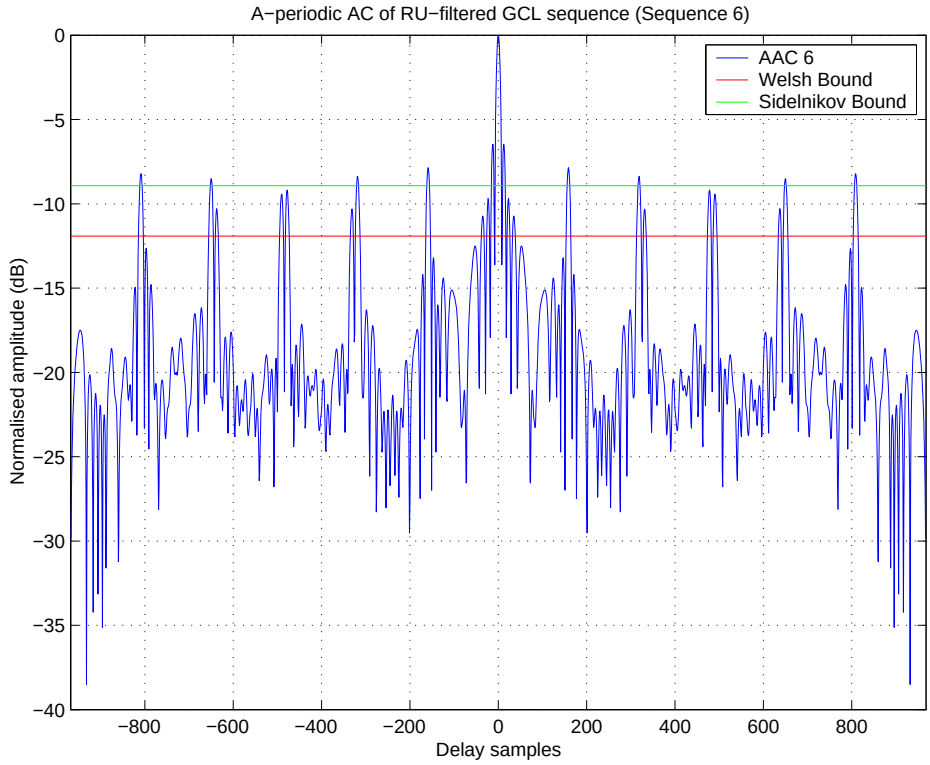

FIGURE 3.14: Aperiodic Auto Correlation (AAC) function of complex spreading sequence 6 in decibels. $(L = 121, RU filtered, spc = 8)$

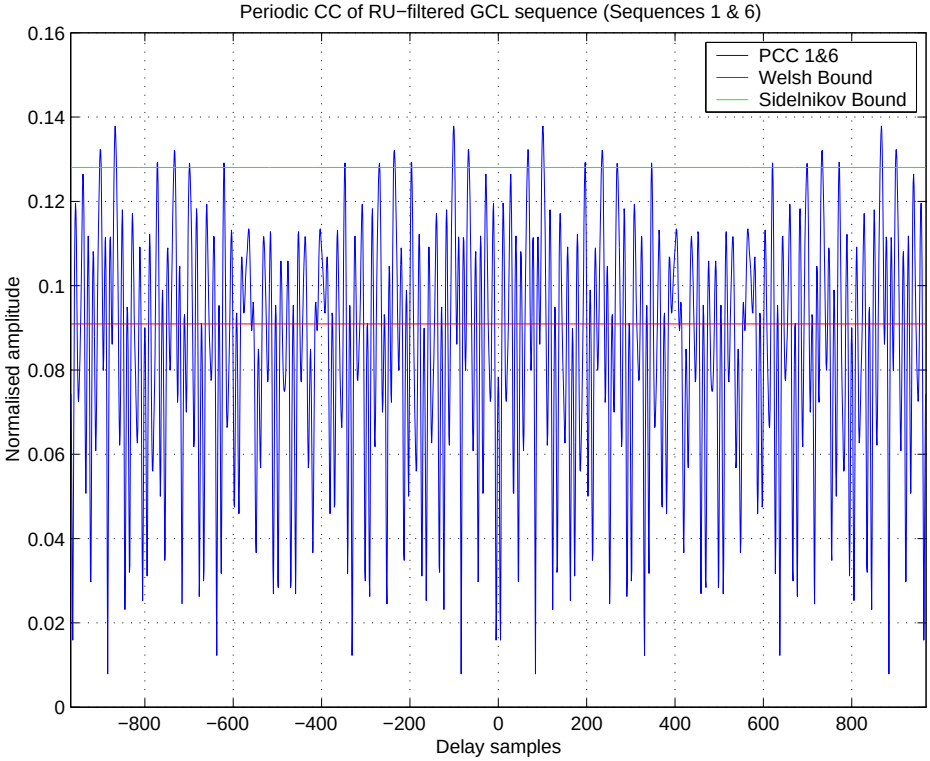

FIGURE 3.15: Periodic Cross Correlation(PCC) function between complex spreading sequences 1 and 6. $(L = 121, RU filtered, spc = 8)$

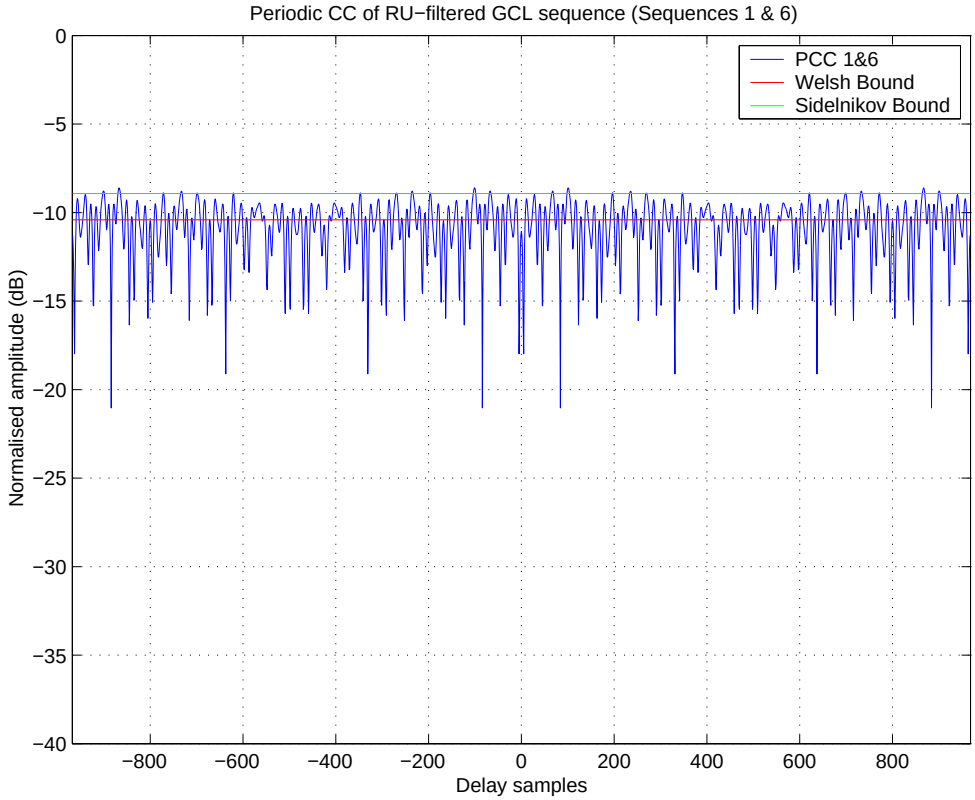

FIGURE 3.16: Periodic Cross Correlation(PCC) function between complex spreading sequences 1 and 6 in decibels. $(L = 121, RUfiltered, spc = 8)$

$$R_{su}[l] = \begin{cases} \sum_{k=0}^{L-1-l} s[l] \cdot u^*[k+l] & ; 0 \leq l \leq L-1 \\ \sum_{k=0}^{L-1+l} s[k-l] \cdot u^*[k] & ; 1-L \leq l < 0 \\ 0 & ; \mid l \mid \geq L \end{cases} \tag{3.19}$$

where * denotes complex conjugate and the time shift is l.

For the ZC sequences the aperiodic CC function is

$$R_{ab}[l] = \begin{cases} \sum_{k=0}^{L-1-l} W_{L_a}^{\frac{k(k+1)}{2}} \cdot W_{L_b}^{\frac{-(k+1)(k+l+1)}{2}} & ; 0 \leq l \leq L-1 \\ \sum_{k=0}^{L-1+l} W_{L_a}^{\frac{(k-l)(k-l+1)}{2}} \cdot W_{L_b}^{\frac{-k(k+l)}{2}} & ; 1-L \leq l < 0 \\ 0 & ; \mid l \mid \geq L \end{cases} \tag{3.20}$$

for $q = 0$ and L odd.

The aperiodic cross correlation functions for the ZC sequences are depicted in Figures 3.17 and 3.18.

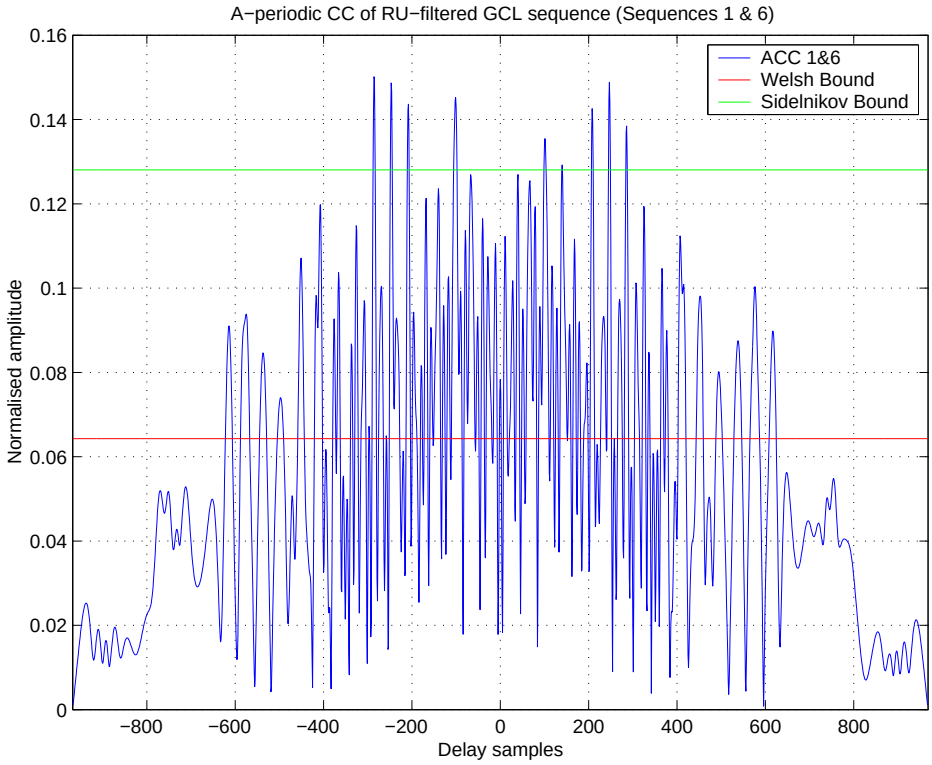

FIGURE 3.17: Aperiodic Cross Correlation(PCC) function between complex spreading sequences 1 and 6. $(L = 121, RU filtered, spc = 8)$

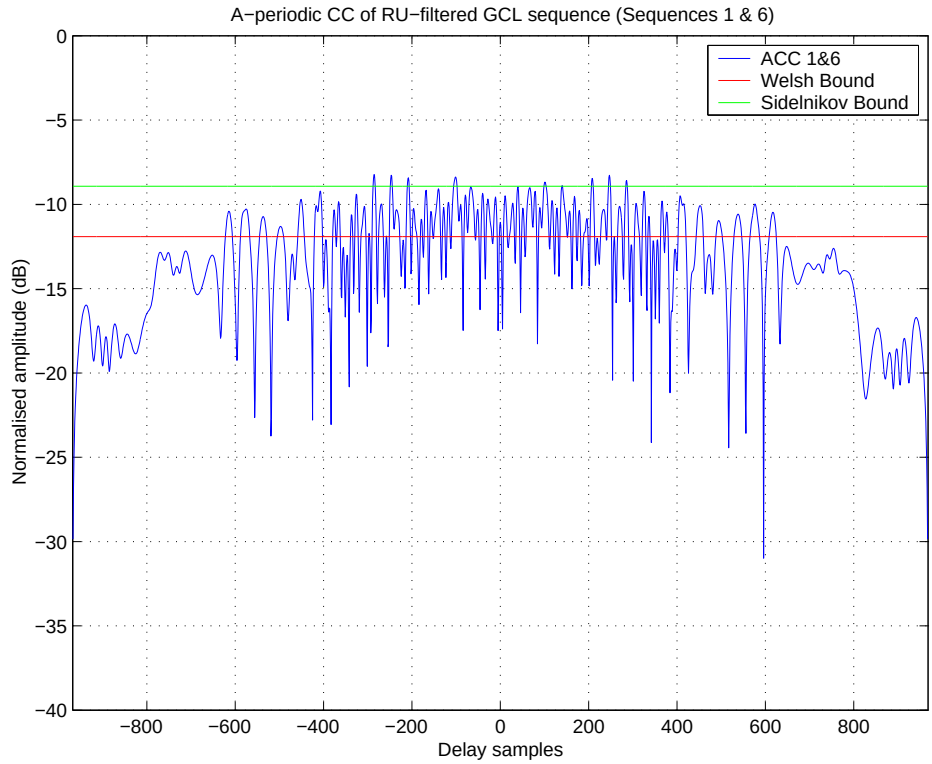

FIGURE 3.18: Periodic Cross Correlation(PCC) function between complex spreading sequences 1 and 6 in decibels. $(L = 121, RU filtered, spc = 8)$

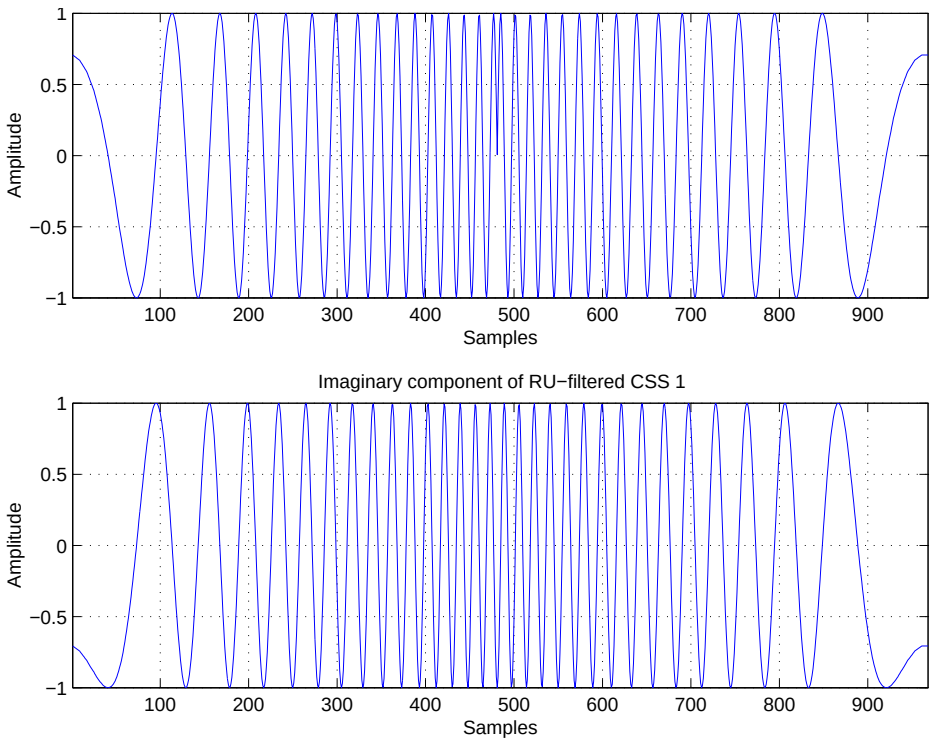

FIGURE 3.19: The Real, (a), and Imaginary, (b), part of the unique combination of CSS 1. $(L = 121, RU filtered, spc = 8)$

Unique combinations of the real and imaginary parts of the complex spreading sequences are used

$$C_{r_1 comb} = C_{r_1} - C_{i_1} \tag{3.21}$$

$$C_{i_1 comb} = -C_{r_1} - C_{i_1} \tag{3.22}$$

and is shown in Figure 3.19.

The same for complex spreading sequence 6

$$C_{r_6 comb} = C_{r_6} - C_{i_6} \tag{3.23}$$

$$C_{i_6 comb} = -C_{r_6} - C_{i_6} \tag{3.24}$$

and is depicted in Figure 3.20.

The auto- and cross correlation functions of these unique combinations are practically identical to the standard Zadoff-Chu correlation functions and are therefore presented in APPENDIX A.

Opperman sequences are closely related to Zadoff-Chu sequences. These sequences are briefly discussed in [34], [35], [36] and [37] for further interest.

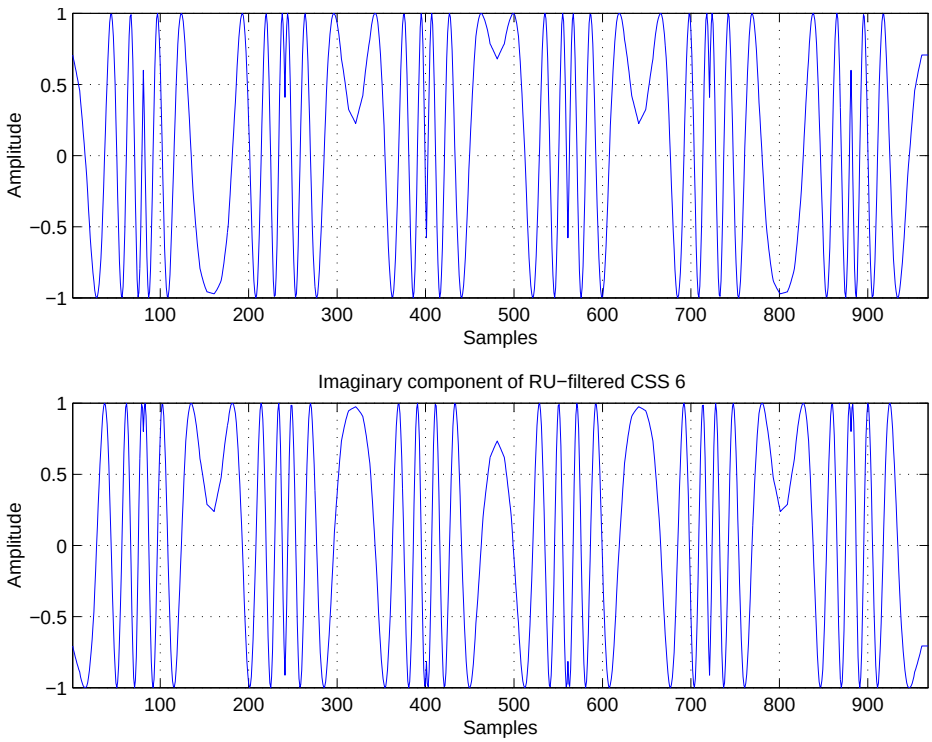

FIGURE 3.20: The Real, (a), and Imaginary, (b), part of the unique combination of CSS 6. $(L = 121, RU filtered, spc = 8)$

3.2.4 Bit Error Probability

In a spread spectrum system the total bit energy is not affected except for its distribution after frequency spreading. In an AWGN environment the spread spectrum modulation provides no gain and thus, the bit error probability will be the same as that of a narrow band system with the same type of modulation scheme. For a BPSK modulated spread spectrum, in an environment which is free of MUI, the average probability of a bit error for equally likely signals is,

$$\begin{aligned} P_e &= \tfrac{1}{2} erfc\left[\sqrt{\tfrac{\alpha^2 E_b}{2 \cdot N_o}(1-\rho_r)}\right] \\ &= Q\left[\sqrt{\tfrac{\alpha^2 E_b}{N_o}(1-\rho_r)}\right] \end{aligned} \tag{3.25}$$

as also given in [21], where α is the channel attenuation, E_b is the energy per bit, N_o the AWGN power spectral density and ρ_r is the correlation coefficient.

By the Central Limit Theorem, in an MUI environment, it is expected that for a large number of users, the MUI will have approximately a Gaussian distribution. With this approximation a simplistic expression is given in [22] for the probability of bit error in a MUI environment. This bit error probability is

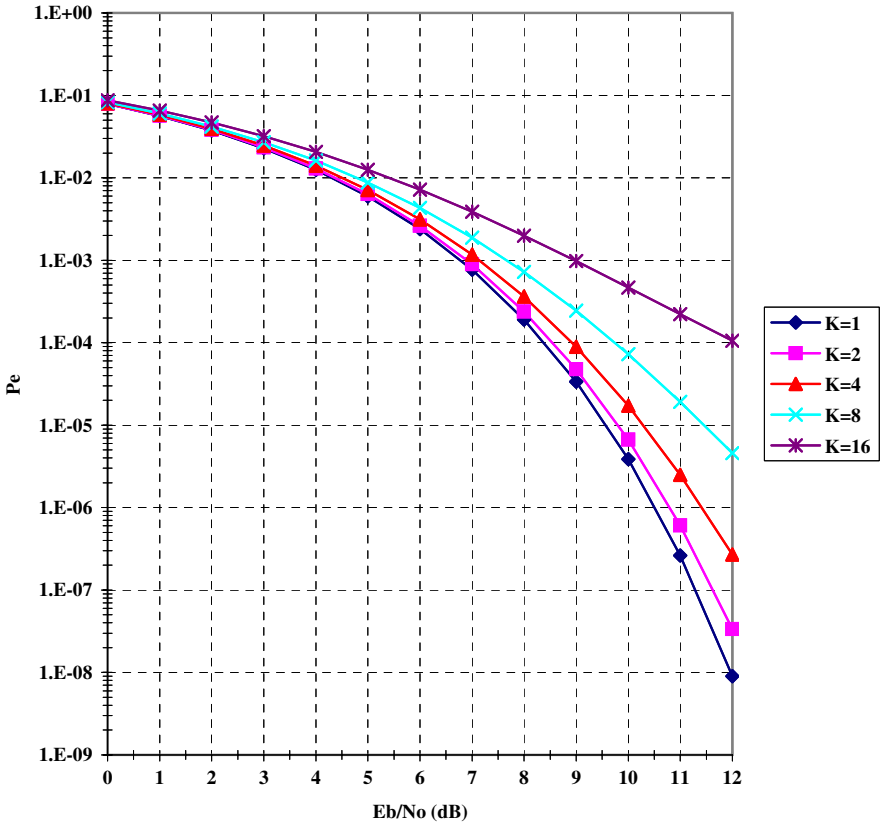

FIGURE 3.21: Bit error probability vs Eb/No for a BPSK/QPSK communication system in an MUI environment for a different number of users.

$$P_e = Q\left[SNR\right] \tag{3.26}$$

where

$$SNR \cong \left[\frac{K-1}{3 \cdot L} + \frac{1}{2}\left(\frac{E_b}{N_o}\right)^{-1}\right]^{-\frac{1}{2}} \tag{3.27}$$

where K is the number of users, L the spreading sequence length, E_b the energy per bit and N_o is the AWGN power spectral density. The bit error probability for a different number of users is depicted in Figure 3.21.

CHAPTER FOUR
DSSS TRANSMITTER

4.1 INTRODUCTION

The power efficiency of the HPA at the transmitter is one of the critical parameters in designing a wireless digital communication system. A constant envelope transmitter output signal requires no input power back-off from the $1dB$ compression point of the HPA, and thus utilizes the power amplifier optimally, ensuring high power efficiency in the transmitter. The balanced as well as the dual channel QPSK transmitters produce constant envelope (CE) outputs, by utilization of the constant envelope non-linearly-interpolated root-of-unity (CE NLI RU) filtered complex spreading sequences (CSS) described in Chapter 3.

Both balanced QPSK and a conventional dual channel QPSK transmitter structures have been investigated, employing unique combinations of the real and imaginary parts of the complex spreading sequences. Utilizing these unique combinations of complex spreading codes in the spreading and despreading processes, ensures optimal operation of the overall system. This advantage will become clear from the theoretical analysis. The theoretical analysis will be done for both balanced and dual-channel quadrature DSSS transmitter structures.

4.2 BALANCED QPSK DSSS TRANSMITTER

In the case of the balanced DSSS transmitter the data on the in-phase (I) and quadrature (Q) branches are identical. The serial incoming data is represented as a complex value and all multiplications in the transmitter are complex. Figure 4.1 shows the block diagram of the complex representation of the balanced DSSS transmitter. The theoretical analysis that

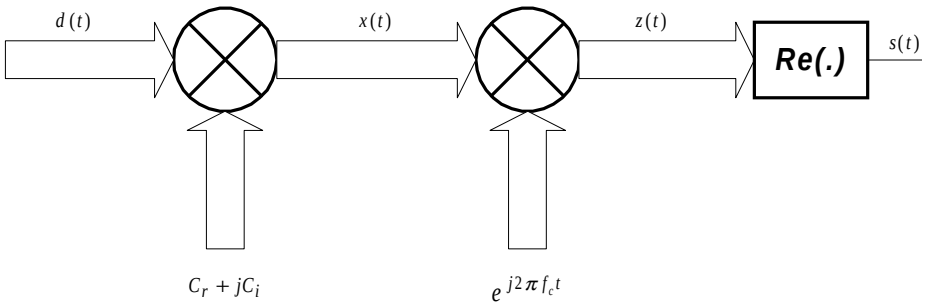

FIGURE 4.1: Block diagram of the balanced DSSS transmitter using complex notation

follows refers to this block diagram.

The input data can be represented as a complex value, namely

$$d(t) = d_1(t) + jd_1(t) \tag{4.1}$$

where $j = \sqrt{-1}$ and $d_1(t)$ denotes the serial input data at bit rate $f_b = \frac{1}{T_b}[bits/s]$, and T_b represents one bit period of a single data bit.

The complex data, $d(t)$ is then spread by multiplying $d(t)$ with a complex spreading sequence $c(t)$, where

$$c(t) = C_r + jC_i \tag{4.2}$$

and Cr denotes the real part of the complex spreading sequence, and Ci denotes the imaginary part of the complex spreading sequence.

The multiplication between $d(t)$ and $c(t)$ results in $x(t)$, i.e.

$$\begin{aligned} x(t) &= d(t) \cdot c(t) \\ &= [d_1(t) + jd_1(t)] \cdot [C_r + jC_i] \\ &= d_1(t) \cdot [C_r - C_i] + jd_1(t) \cdot [C_r + C_i] \end{aligned} \tag{4.3}$$

$x(t)$ is then modulated onto a carrier $e^{j2\pi f_c t}$, where f_c is the carrier frequency, to obtain the modulated signal, $z(t)$,

$$\begin{aligned} z(t) &= x(t) \cdot e^{j2\pi f_c t} \\ &= \{d_1(t) \cdot [C_r - C_i] + jd_1(t) \cdot [C_r + C_i]\} \cdot e^{j2\pi f_c t} \\ &= \{d_1(t) \cdot [C_r - C_i] \cdot cos(2\pi f_c t) - d_1(t) \cdot [C_r + C_i] \cdot sin(2\pi f_c t)\} \\ &\quad + j\{d_1(t) \cdot [C_r - C_i] \cdot sin(2\pi f_c t) + d_1(t) \cdot [C_r + C_i] \cdot cos(2\pi f_c t)\} \end{aligned} \quad (4.4)$$

The final output signal, $s(t)$, of the DSSS transmitter is obtained by taking the real part of $z(t)$, giving

$$\begin{aligned} s(t) &= Re\{z(t)\} \\ &= d_1(t) \cdot [C_r - C_i] \cdot cos(2\pi f_c) - d_1(t) \cdot [C_r + C_i] \cdot sin(2\pi f_c t) \end{aligned} \quad (4.5)$$

$s(t)$ can be represented in complex notation as

$$s(t) = Re\{u_1 \cdot e^{j2\pi f_c t}\} + Re\{ju_2 \cdot e^{j2\pi f_c t}\} \quad (4.6)$$

where

$$u_1(t) = d_1(t) \cdot [C_r - C_i] \quad (4.7)$$

and

$$u_2(t) = d_1(t) \cdot [C_r + C_i] \quad (4.8)$$

Figure 4.2 depicts an equivalent structure for the balanced DSSS transmitter shown in Figure 4.1.

The envelope of the balanced QPSK DSSS transmitter output signal can be written as

$$\begin{aligned} e(t) &= \sqrt{(x_1^2(t) + x_2^2(t))} \\ &= \sqrt{(d_1(t) \cdot [C_r - C_i])^2 + (d_1(t) \cdot [-C_r - C_i])^2} \\ &= \sqrt{(d_1^2(t) \cdot [C_r - C_i]^2) + (d_2^1(t) \cdot [-C_r - C_i]^2)} \\ &= \sqrt{(C_r C_r - 2C_r C_i + C_i C_i) + (C_r C_r + 2C_r C_i + C_i C_i)} \\ &= \sqrt{2} \cdot \sqrt{C_r^2 + C_i^2} \\ &= \sqrt{2} \end{aligned} \quad (4.9)$$

where $d_1^2(t) = 1$ and $C_r^2 + C_i^2 = 1$.

Equation 4.9 shows that the envelope of the output signal of the balanced QPSK DSSS transmitter is constant and the phase trajectory of the output is restrained to only traverse the unit circle.

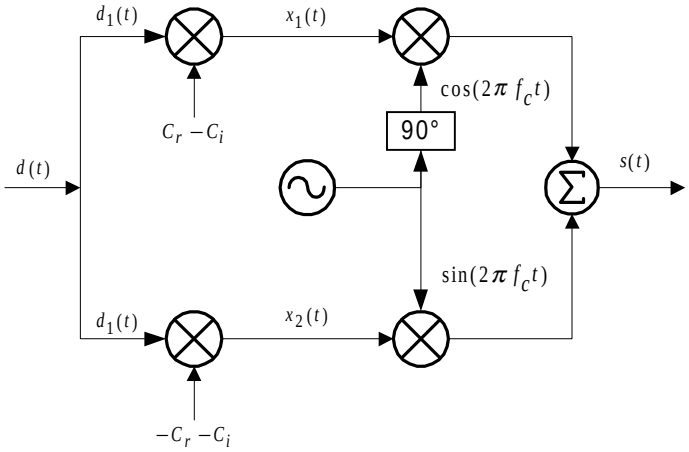

FIGURE 4.2: Block diagram of the balanced DSSS transmitter using real notation, suitable for direct implementation

4.3 DUAL CHANNEL QPSK DSSS TRANSMITTER

The dual channel QPSK transmitter has independent parallel data streams on the in-phase and quadrature branches. A direct realization is depicted in Figure 4.3.

Firstly the incoming serial data is converted into two parallel streams, $x_1(t)$ and $x_2(t)$, respectively. These two parallel data streams are then spread by means of unique combinations of complex spreading sequences, C_I and C_Q, as defined in Chapter 3.

$$x_1(t) = d_1(t) \cdot [C_r - C_i] \tag{4.10}$$

and

$$x_2(t) = d_2(t) \cdot [-C_r - C_i] \tag{4.11}$$

$x_1(t)$ and $x_2(t)$ are then modulated onto cosine and sine carriers and summed to form the final output signal, $s(t)$, of the dual channel QPSK DSSS transmitter, which can be written as:

$$\begin{aligned} s(t) &= x_1(t) \cdot \cos(2\pi f_c t) + x_2(t) \cdot \sin(2\pi f_c t) \\ &= d_1(t) \cdot [C_r - C_i] \cdot \cos(2\pi f_c t) \\ &+ d_2(t) \cdot [-C_r - C_i] \cdot \sin(2\pi f_c t) \end{aligned} \tag{4.12}$$

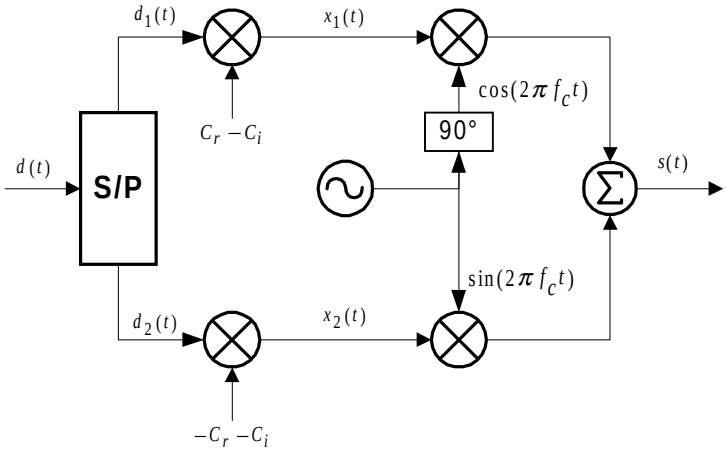

FIGURE 4.3: Block diagram of the QPSK DSSS transmitter

The envelope of the dual channel DSSS QPSK output signal can be written as:

$$\begin{aligned} e(t) &= \sqrt{(x_1^2(t) + x_2^2(t))} \\ &= \sqrt{(d_1(t) \cdot [C_r - C_i])^2 + (d_2(t) \cdot [-C_r - C_i])^2} \\ &= \sqrt{(d_1^2(t) \cdot [C_r - C_i]^2) + (d_2^2(t) \cdot [-C_r - C_i]^2)} \\ &= \sqrt{(C_r C_r - 2C_r C_i + C_i C_i) + (C_r C_r + 2C_r C_i + C_i C_i)} \\ &= \sqrt{2} \cdot \sqrt{C_r^2 + C_i^2} \\ &= \sqrt{2} \end{aligned} \tag{4.13}$$

where $d_1^2(t) = 1$, $d_2^2(t) = 1$ and $C_r^2 + C_i^2 = 1$.

The dual channel DSSS QPSK transmitter's output signal exhibits a constant envelope, as can be deducted from Equation 4.13.

CHAPTER FIVE
DSSS RECEIVER

5.1 INTRODUCTION

Different receiver structures were investigated in the search for an optimum configuration for the proposed DSSS communication system, employing complex spreading sequences. The receiver structures have been designed to demodulate and despread transmitter signals corresponding to the balanced and dual-channel transmitter configurations, respectively, as described in Chapter 4. The following sections give a detailed analysis of these receiver structures. In the theoretical analysis presented in this chapter only the effects of AWGN will be taken into account. The corresponding effects of phase and timing errors will be addressed in the synchronization section in Chapter 6.

5.2 BALANCED QPSK DSSS RECEIVER

A block diagram of the balanced DSSS receiver structure is depicted in Figure 5.1 and the theoretical analysis that follows refers to this block diagram.

The received signal, $r(t)$, at the input of the balanced DSSS receiver, can be written as

$$r(t) = d_1(t) \cdot C_I \cdot \cos(2\pi f_c t) + d_1(t) \cdot C_Q \cdot sin(2\pi f_c t) + n(t) \tag{5.1}$$

where C_I and C_Q are the data-synchronous in-phase and quadrature-phase combinations of the real and imaginary parts of the CSS, respectively. $n(t)$ denotes bandlimited AWGN with double-sided power spectral density $N_o/2$, which can be written as

$$n(t) = n_c(t)\cos(2\pi f_c t) - n_s(t)\sin(2\pi f_c t) \tag{5.2}$$

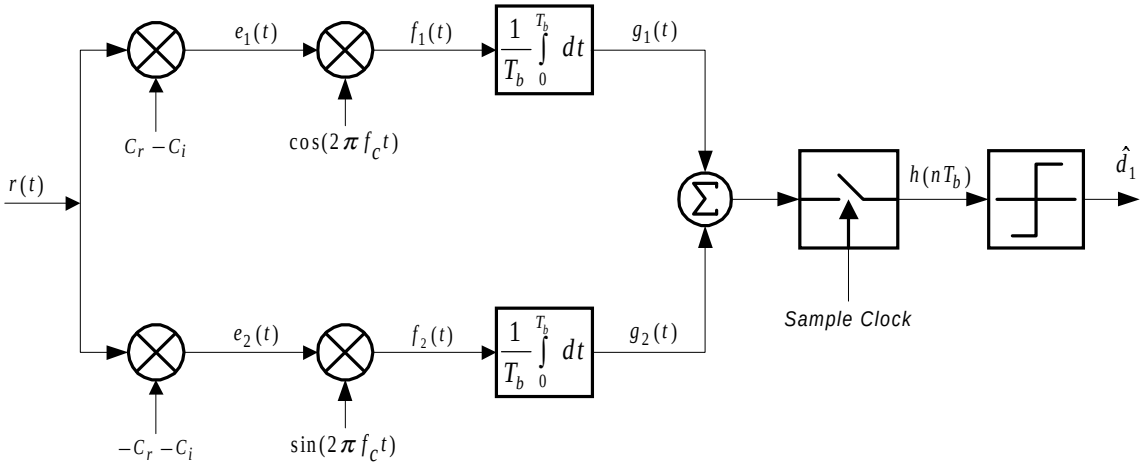

FIGURE 5.1: Block diagram of the balanced DSSS receiver

The incoming signal is split into two parallel branches which are despread with the unique complex spreading sequence combinations, C_I and C_Q. These despread in-phase and quadrature branches are then demodulated with the recovered cosine and sine carriers, to obtain $f_1(t)$ and $f_2(t)$, respectively.

Consider $f_1(t)$:

$$\begin{aligned} f_1(t) &= r(t) \cdot C_I \cos(2\pi f_c t)) \\ &= \frac{1}{2} d_1(t) \cdot C_I C_I \cdot [1 + \cos(4\pi f_c t)] + \frac{1}{2} d_1(t) \cdot C_Q C_I \cdot \sin(4\pi f_c t) \\ &+ \frac{1}{2} n_c(t) C_I \cdot [1 + \cos(4\pi f_c t)] - \frac{1}{2} n_s(t) C_I \cdot \sin(4\pi f_c t) \end{aligned} \tag{5.3}$$

and $f_2(t)$:

$$\begin{aligned} f_2(t) &= r(t) \cdot C_Q \sin(2\pi f_c t)) \\ &= \frac{1}{2} d_1(t) \cdot C_I C_Q \cdot \sin(4\pi f_c t) + \frac{1}{2} d_1(t) \cdot C_Q C_Q \cdot [1 - \cos(4\pi f_c t)] \\ &+ \frac{1}{2} n_c(t) C_Q \cdot \sin(4\pi f_c t) - \frac{1}{2} n_s(t) C_Q \cdot [1 - \cos(4\pi f_c t)] \end{aligned} \tag{5.4}$$

In order to eliminate the high frequency components of the mixing process, both branch signals are integrate-and-dumped to obtain $g_1(t)$ and $g_2(t)$,

$$g_1(t) = \frac{1}{2T_b} \int_0^{T_b} \{d_1(t) \cdot C_I C_I + n_c(t) C_I\}\, dt \tag{5.5}$$

$$g_2(t) = \frac{1}{2T_b} \int_0^{T_b} \{d_1(t) \cdot C_Q C_Q - n_s(t) C_Q\}\, dt \tag{5.6}$$

With $d_1(t) \in \{-1; 1\}$,

$$\omega_{c_I}(t) = \frac{1}{2T_b} \int_0^{T_b} n_c(t) C_I \, dt, \tag{5.7}$$

$$\omega_{s_Q}(t) = \frac{1}{2T_b} \int_0^{T_b} n_s(t) C_Q \, dt \tag{5.8}$$

Thus,

$$g_1(t) = \frac{d_1(t)}{2T_b} \int_0^{T_b} C_I C_I \, dt + \omega_{c_I}(t) \tag{5.9}$$

and

$$g_2(t) = \frac{d_1(t)}{2T_b} \int_0^{T_b} C_Q C_Q \, dt - \omega_{s_Q}(t) \tag{5.10}$$

Both branches, $g_1(t)$ and $g_2(t)$ can be summed because of the balanced structure at the transmitter, yielding identical data on both branches, whereafter a sample-and-hold operation is performed (at time instants $t = nT_b$ for $n = 0, 1, 2, ...$), to obtain

$$\begin{aligned} h(nT_b) &= \frac{1}{T_b} d_1(nT_b) \int_0^{T_b} \{C_r C_r + C_i C_i\} \, dt + \omega_{c_I}(nT_b) - \omega_{s_Q}(nT_b) \\ &= \frac{N}{T_b} d_1(nT_b) + \omega_{c_I}(nT_b) - \omega_{s_Q}(nT_b) \end{aligned} \tag{5.11}$$

where it is assumed that there is zero time shift between the incoming spreading codes and the despreading codes at the receiver. Finally, signal detection is performed on $h(nT_b)$ to recover the original data, $\hat{d_1}$.

5.3 DUAL CHANNEL QPSK DSSS RECEIVER

The block diagram of the dual channel QPSK DSSS receiver structure is shown in Figure 5.2 and the theoretical analysis that follows refers to this block diagram.

The received signal, $r(t)$, at the input of the DSSS QPSK receiver can be written as

$$r(t) = d_1(t) \cdot C_I \cdot cos(2\pi f_c) + d_2(t) \cdot C_Q \cdot sin(2\pi f_c t) + n(t) \tag{5.12}$$

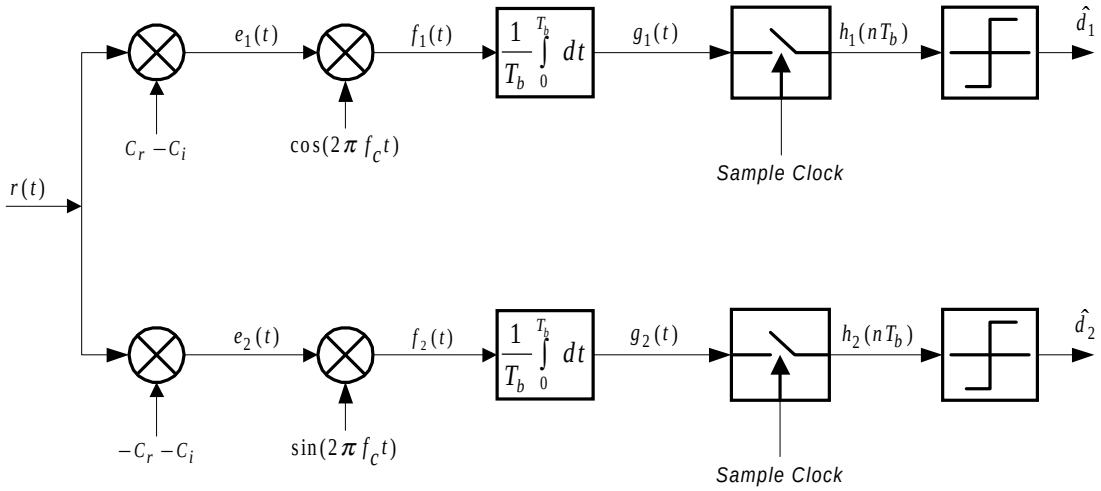

FIGURE 5.2: Block diagram of the QPSK DSSS receiver

where C_I and C_Q are the data-synchronous in-phase and quadrature-phase combinations of the real and imaginary parts of the CSS, respectively. $n(t)$ denotes bandlimited AWGN with double-sided power spectral density $N_o/2$, and can be written as

$$n(t) = n_c(t)\cos(2\pi f_c) - n_s(t)\sin(2\pi f_c t) \tag{5.13}$$

The incoming signal is split into two parallel branches, despread with C_I and C_Q and multiplied with the recovered cosine and sine carriers, to obtain $f_1(t)$ and $f_2(t)$, respectively.

This yields

$$\begin{aligned} f_1(t) &= r(t)\cdot C_I\cos(2\pi f_c t)) \\ &= \frac{1}{2}d_1(t)\cdot C_I C_I\cdot[1+\cos(4\pi f_c t)] + \frac{1}{2}d_2(t)\cdot C_Q C_I\cdot\sin(4\pi f_c t) \\ &+ \frac{1}{2}n_c(t)C_I\cdot[1+\cos(4\pi f_c t)] - \frac{1}{2}n_s(t)C_I\cdot\sin(4\pi f_c t) \end{aligned} \tag{5.14}$$

and

$$\begin{aligned} f_2(t) &= r(t)\cdot C_Q\sin(2\pi f_c t)) \\ &= \frac{1}{2}d_1(t)\cdot C_I C_Q\cdot\sin(4\pi f_c t) + \frac{1}{2}d_2(t)\cdot C_Q C_Q\cdot[1-\cos(4\pi f_c t)] \\ &+ \frac{1}{2}n_c(t)C_Q\cdot\sin(4\pi f_c t) - \frac{1}{2}n_s(t)C_Q\cdot[1-\cos(4\pi f_c t)] \end{aligned} \tag{5.15}$$

In order to eliminate the high frequency components, both branch signals are

integrate-and-dumped to obtain $g_1(t)$ and $g_2(t)$,

$$g_1(t) = \frac{1}{2T_b}\int_0^{T_b} d_1(t)\cdot C_I C_I\,dt + \frac{1}{2T_b}\int_0^{T_b} n_c(t)C_I\,dt \tag{5.16}$$

$$g_2(t) = \frac{1}{2T_b}\int_0^{T_b} d_2(t)\cdot C_Q C_Q\,dt - \frac{1}{2T_b}\int_0^{T_b} n_s(t)C_Q\,dt \tag{5.17}$$

With $d_1(t) \in \{-1;1\}$, $d_2(t) \in \{-1;1\}$,

$$\omega_{c_I}(t) = \frac{1}{2T_b}\int_0^{T_b} n_c(t)C_I\,dt, \tag{5.18}$$

$$\omega_{s_Q}(t) = \frac{1}{2T_b}\int_0^{T_b} n_s(t)C_Q\,dt \tag{5.19}$$

Note that at zero time shift,

$$\frac{1}{T_b}\int_0^{T_b} C_I C_I\,dt \approx \frac{N}{T_b} \tag{5.20}$$

and

$$\frac{1}{T_b}\int_0^{T_b} C_Q C_Q\,dt \approx \frac{N}{T_b} \tag{5.21}$$

Equation 5.16 and 5.17 reduces to

$$g_1(t) = \frac{Nd_1(t)}{2T_b} + \omega_{c_I}(t) \tag{5.22}$$

and

$$g_2(t) = \frac{Nd_2(t)}{2T_b} - \omega_{s_Q}(t) \tag{5.23}$$

$g_1(t)$ and $g_2(t)$ are then sample-and-hold at time instants $t = nT_b$ for $n = 0, 1, 2, ...$, to obtain

$$h_1(nT_b) = \frac{Nd_1(nT_b)}{2T_b} + \omega_{c_I}(nT_b) \tag{5.24}$$

$$h_2(nT_b) = \frac{Nd_2(nT_b)}{2T_b} - \omega_{s_Q}(nT_b) \tag{5.25}$$

Signal detection is performed on $h_1(nT_b)$ and $h_2(nT_b)$ to recover the original data signals, $\hat{d}_1$ and $\hat{d}_2$, after which a parallel-to-serial conversion is done to recover an estimate of the original serial data stream, $\hat{d}(t)$.

CHAPTER SIX
SYNCHRONIZATION

6.1 INTRODUCTION

In a spread-spectrum communication link several levels of synchronization have to be maintained between the transmitter and the receiver. These synchronization subsystems can be subdivided into temporal and carrier synchronization classes. The initial time synchronization subsystem is responsible for the determination of the initial code phase of the received spread-spectrum signal, and the corresponding process is called *code acquisition*. The function of second temporal synchronisation phase is to maintain code synchronization after initial code acquisition has been accomplished, and is called *code tracking*. Carrier synchronization comprises *initial carrier acquisition* and *carrier phase tracking*. All of these above mentioned components of synchronization needs to function jointly and optimally to deliver a spread-spectrum system with reliable performance. The synchronization of a DSSS communication system employing complex spreading sequences will be investigated and designed in this chapter, constituting one of the main novel contributions of this dissertation, apart of the hardware implementation of the complete system.

A DSSS system requires excellent synchronization for code acquisition, code tracking and carrier synchronization to ensure best system performance and to minimize multi-user interference. Code tracking loops and demodulation receiver structures for spread-spectrum systems can be categorised in coherent and non-coherent tracking loops and receiver structures. Coherent receiver loops make use of received carrier phase information, whereas non-coherent receiver loops do not. In this DSSS communication system, employing complex spreading sequences, synchronization structures for code acquisition and code

tracking as well as carrier tracking and data demodulation will be investigated and designed by using a coherent approach. The reason for utilizing coherent detection and tracking loop structures is because of the advantage in system performance of the coherent receiver compared to the non-coherent receiver structures.

A combined coherent Decision-Directed Costas Carrier Recovery Loop (DD-CCRL) and Coherent Decision-Directed Complex Delay-Lock-Loop (DD-CDLL) synchronization scheme for a DSSS communication system, originally proposed by De Gaudenzi et al [8] for systems using binary spreading sequences, have been generalized and extended to include systems employing binary and/or complex spreading sequences. In addition to its versatility, other major advantages offered by this unique code locking scheme are that it eliminates the problem of arm imbalance by obviating the need for squaring devices in the loop structure. The absence of the latter leads to improved tracking ability. The new structure also facilitates simplified hardware by requiring only two loop correlators in stead of four, such as required for non-coherent DLL schemes in the case of complex spreading sequences. This simplified structure is obtained through the novel use of composite signals in the spreading, despreading and code locking processes, which leads to effective cancellation of unwanted cross product interference terms, generated in the said processes.

6.2 GLOBAL RECEIVER STRUCTURE

The global DSSS synchronization scheme is depicted in Figure 6.1. The receiver synchronization structure consists of three modules running in parallel. These modules are the acquisition circuitry [38], shown in Figure 6.4, consisting of a coherent Decision-Directed Costas Carrier-Recovery-Loop (DD-CCRL), shown in Figures 6.2 and 6.3, and a novel coherent Decision-Directed Complex Delay-Lock-Loop (DD-CDLL) depicted in Figures 6.5 and 6.9, for the balanced QPSK and dual channel QPSK configurations, respectively. Initial synchronization is performed by the acquisition circuitry. Prior to acquisition the transmit and receive complex sequence generators are not in synchronism, that is, the zero reference time positions of the complex spreading sequences are not aligned. In order to achieve code locking, a course sliding correlation [38] is first performed on the in-phase and quadrature phase branches. The outputs of the sliding correlators are then used to determine when the spreading code and the despreading code are aligned within one chip period. During the initial synchronization time the coherent DD-CDLL is in an open loop free running mode. Once the alignment of the spreading

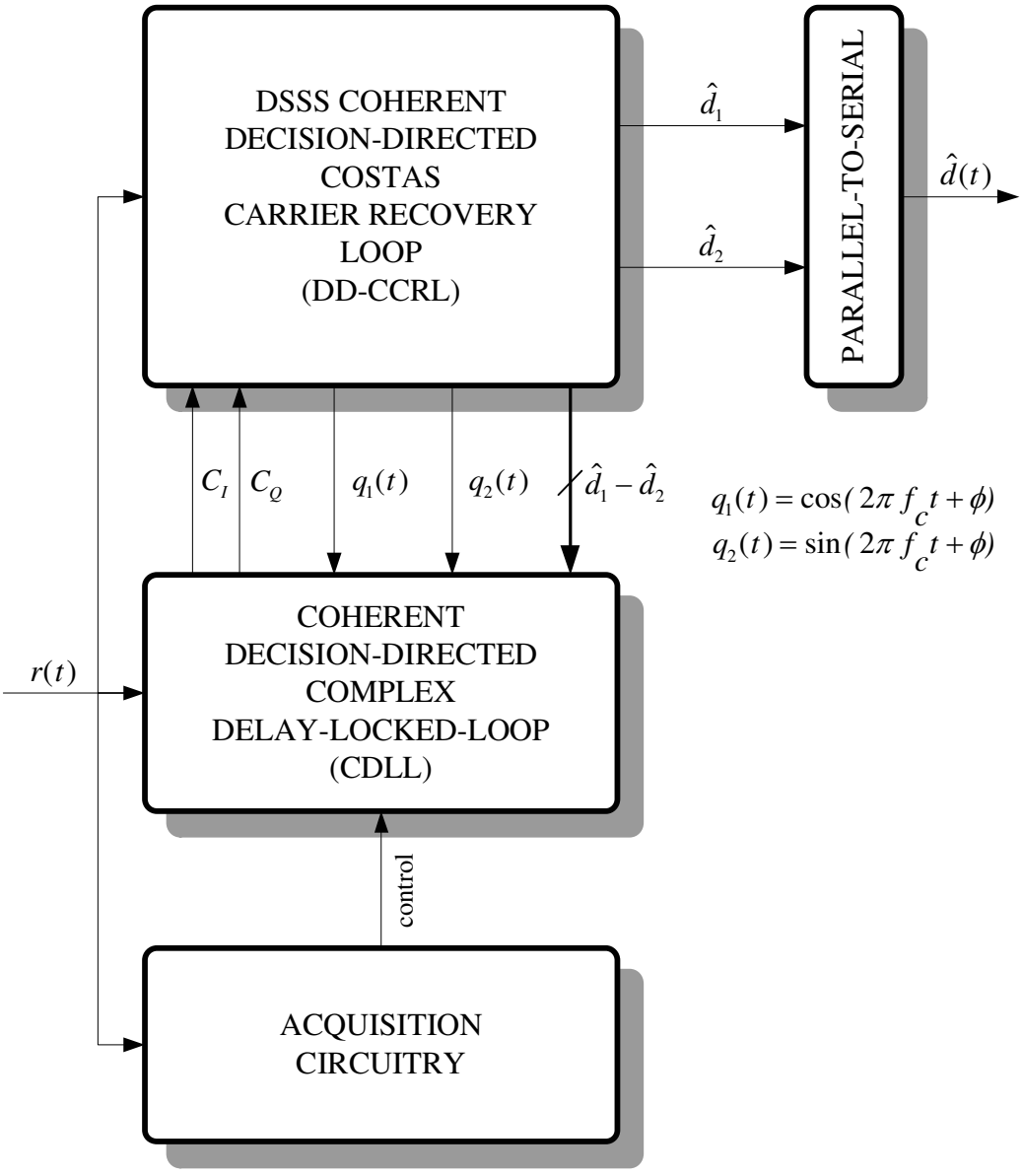

FIGURE 6.1: Block diagram of the global DSSS receiver structure

and despreading codes are detected to be within one chip period, the coherent DD-CDLL is switched to a closed loop mode for code tracking. Consequently, the receiver complex spreading sequence generator is aligned to within one chip period with the transmitted spreading sequence.

The operation of the coherent DD-CDLL commences immediately after course synchronization (acquisition) has been achieved. Code tracking or fine synchronization is performed by the coherent DD-CDLL. The coherent DD-CDLL provides the synchronized punctual composite signals of the real and imaginary parts of the CSS to the DD-CCRL to perform carrier tracking. The same punctual composite signals are also fed to the despreading and data detection subsystems, to facilitate recovery of the original data streams. The received DSSS signal is correlated with composite signals, consisting of the difference between the early and late replicas of unique combinations of the real and imaginary parts of a CSS, on the in-phase and quadrature phase branches, respectively. The correlation results are converted to baseband by means of the recovered cosine and sine carriers, provided by the DD-CCRL. The data modulation on the two branches is eliminated by means of the decisions made in the DD-CCRL and then combined to derive a proper loop error signal to drive the Numerically Controlled Code Generator (NCCG). The major advantage of this unique structure of the coherent DD-CDLL is that it eliminates the problem of arm imbalance. It simplifies and reduces the hardware that would have been required to realise four correlators, to the hardware required to implement only two correlators, and also improves the tracking capabilities of the loop, because of the absence of squaring devices (commonly found in non-coherent DLL schemes).

The DD-CCRL provides recovered sine and cosine carriers to demodulate the incoming signal to a specific intermediate frequency (IF). Despreading of the incoming signal forms part of the DD-CCRL. Despreading is also done by means of the same unique combinations of real and imaginary parts of the complex spreading sequences used at the transmitter, ensuring optimal performance through the elimination of unwanted cross product interference terms. Data decisions are made on the despreaded in-phase and quadrature branches and are used to eliminate the data modulation on the despreaded branches to generate an error signal for controlling the NCO that provides the recovered quadrature carriers.

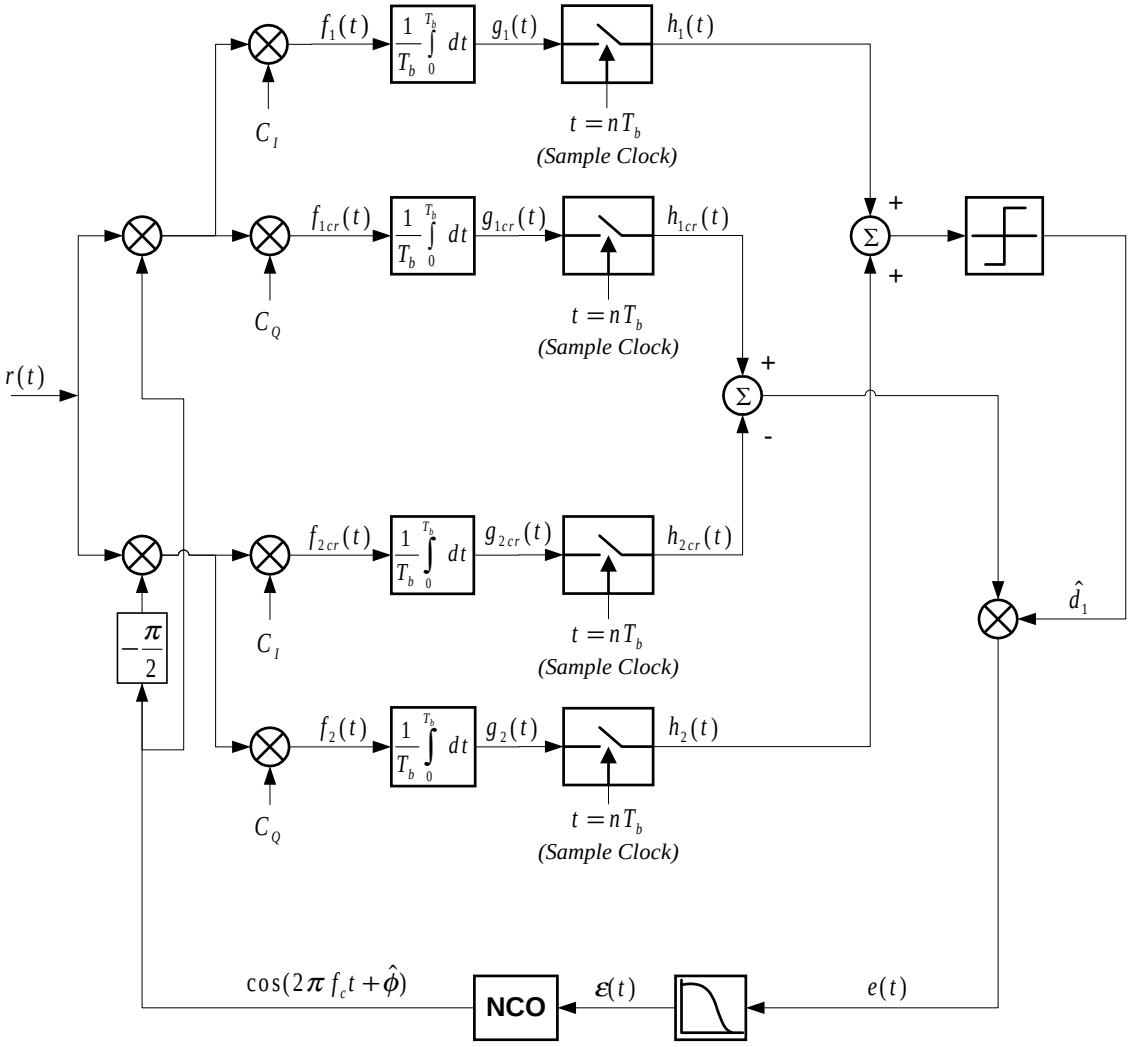

FIGURE 6.2: Block diagram of the Balanced QPSK Coherent Complex Decision-Directed Costas Carrier Recovery Loop

6.3 CARRIER AND PHASE SYNCHRONIZATION

In this section the coherent DD-CCRLs will be analyzed for both the balanced QPSK and dual channel QPSK DSSS communication systems.

6.3.1 Balanced QPSK Coherent Complex Decision-Directed Costas Carrier Recovery Loop

Figure 6.2 shows the block diagram of the coherent complex DD-CCRL used for carrier tracking in the balanced QPSK DSSS configuration.

With reference to Figure 6.2, the input signal $r(t)$, on a specific IF at the input of the

balanced QPSK DSSS receiver, can be written as

$$r(t) = d_1(t) \cdot C_I \cdot \cos(2\pi f_c t + \phi) - d_1(t) \cdot C_Q \cdot sin(2\pi f_c t + \phi) + n(t) \tag{6.1}$$

where C_I and C_Q are the data-synchronous in-phase and quadrature-phase combinations of the real and imaginary parts of the CSS, respectively. $n(t)$ denotes bandlimited AWGN with double-sided power spectral density $N_o/2$, which can be written as

$$n(t) = n_c(t)\cos(2\pi f_c t + \phi) - n_s(t)\sin(2\pi f_c t + \phi) \tag{6.2}$$

The incoming signal is demodulated with an estimate of the incoming quadrature carriers and despread with synchronized despreading sequences to produce a despread baseband signal, as well as high frequency components on the in-phase and quadrature branch, given by

$$\begin{aligned} f_{1cr}(t) &= \frac{d_1(t)C_I C_Q}{2}\left[\cos(4\pi f_c t + \phi + \hat{\phi}) + \cos(\phi - \hat{\phi})\right] \\ &- \frac{d_1(t)C_Q C_Q}{2}\left[\sin(4\pi f_c t + \phi + \hat{\phi}) + \sin(\phi - \hat{\phi})\right] \\ &+ \frac{n_c(t)C_Q}{2}\left[\cos(4\pi f_c t + \phi + \hat{\phi}) + \cos(\phi - \hat{\phi})\right] \\ &- \frac{n_s(t)C_Q}{2}\left[\sin(4\pi f_c t + \phi + \hat{\phi}) + \sin(\phi - \hat{\phi})\right] \end{aligned} \tag{6.3}$$

on the in-phase branch and

$$\begin{aligned} f_{2cr}(t) = &- \frac{d_1(t)C_I C_I}{2}\left[\sin(4\pi f_c t + \phi + \hat{\phi}) - \sin(\phi - \hat{\phi})\right] \\ &+ \frac{d_1(t)C_I C_Q}{2}\left[\cos(\phi - \hat{\phi}) - \cos(4\pi f_c t + \phi + \hat{\phi})\right] \\ &- \frac{n_c(t)C_I}{2}\left[\sin(4\pi f_c t + \phi + \hat{\phi}) - \sin(\phi - \hat{\phi})\right] \\ &+ \frac{n_s(t)C_I}{2}\left[\cos(\phi - \hat{\phi}) - \cos(4\pi f_c t + \phi + \hat{\phi})\right] \end{aligned} \tag{6.4}$$

on the quadrature branch.

In order to eliminate the high frequency components and conclude the despreading process, both branch signals are integrate-and-dumped to obtain $g_1(t)$ and $g_2(t)$, respectively:

$$g_{1cr}(t) = \frac{d_1(t)\cos(\phi - \hat{\phi})}{2T_b}\int_0^{T_b} C_I C_Q dt$$

$$
\begin{aligned}
& - \frac{d_1(t)\sin(\phi-\hat{\phi})}{2T_b}\int_0^{T_b} C_Q C_Q dt \\
& + \frac{\cos(\phi-\hat{\phi})}{2T_b}\int_0^{T_b} n_c(t) C_Q dt \\
& - \frac{\sin(\phi-\hat{\phi})}{2T_b}\int_0^{T_b} n_s(t) C_Q dt
\end{aligned} \tag{6.5}
$$

$$
\begin{aligned}
g_{2cr}(t) &= \frac{d_1(t)\sin(\phi-\hat{\phi})}{2T_b}\int_0^{T_b} C_I C_I dt \\
&+ \frac{d_1(t)\cos(\phi-\hat{\phi})}{2T_b}\int_0^{T_b} C_I C_Q dt \\
&+ \frac{\sin(\phi-\hat{\phi})}{2T_b}\int_0^{T_b} n_c(t) C_I dt \\
&+ \frac{\cos(\phi-\hat{\phi})}{2T_b}\int_0^{T_b} n_s(t) C_I dt
\end{aligned} \tag{6.6}
$$

Noting that $d_1(t) \in \{-1; 1\}$ and

$$\omega_{c_I}(t) = \frac{1}{2T_b}\int_0^{T_b} n_c(t) C_I \, dt, \tag{6.7}$$

$$\omega_{c_Q}(t) = \frac{1}{2T_b}\int_0^{T_b} n_c(t) C_Q \, dt, \tag{6.8}$$

$$\omega_{s_I}(t) = \frac{1}{2T_b}\int_0^{T_b} n_s(t) C_I \, dt \tag{6.9}$$

$$\omega_{s_Q}(t) = \frac{1}{2T_b}\int_0^{T_b} n_s(t) C_Q \, dt \tag{6.10}$$

equations 6.5 and 6.6 can be written as

$$
\begin{aligned}
g_{1cr}(t) &= \frac{d_1(t)\cos(\phi-\hat{\phi})}{2T_b}\int_0^{T_b} C_I C_Q dt \\
&- \frac{d_1(t)\sin(\phi-\hat{\phi})}{2T_b}\int_0^{T_b} C_Q C_Q dt
\end{aligned}
$$

$$+ \quad \omega_{cQ}(t)\cos(\phi-\hat{\phi})$$

$$- \quad \omega_{sQ}(t)\sin(\phi-\hat{\phi}) \tag{6.11}$$

and

$$\begin{aligned} g_{2cr}(t) &= \frac{d_1(t)\sin(\phi-\hat{\phi})}{2T_b}\int_0^{T_b} C_I C_I dt \\ &+ \frac{d_1(t)\cos(\phi-\hat{\phi})}{2T_b}\int_0^{T_b} C_I C_Q dt \\ &+ \omega_{cI}(t)\sin(\phi-\hat{\phi}) \\ &+ \omega_{sI}(t)\cos(\phi-\hat{\phi}) \end{aligned} \tag{6.12}$$

The outputs of the integrate-and-dump blocks are sample-and-hold at optimum time instants at the end of each integration period (i.e., at time instants $t = nT_b$ for $n = 0, 1, 2, ...$).

The quadrature samples are subtracted from the in-phase samples and the result is multiplied by the data decision, $\hat{d}_1$, provided by the despreading and data detection processes. This is done to produce an DD-CCRL error signal without any data modulation. This concept is based on a decision-directed method and has the advantage of eliminating the additional noise from the tracking loop caused by data modulation (so-called data-dependent noise). The error signal is given by

$$\begin{aligned} e(nT_b) = &- \frac{1}{2T_b}\int_0^{T_b}\left[C_I C_I + C_Q C_Q\right]dt \cdot \sin(\phi-\hat{\phi}) \\ &+ \left[\omega_{cQ}(nT_b) - \omega_{sI}(nT_b)\right]\sin(\phi-\hat{\phi}) \\ &- \left[\omega_{sI}(nT_b) + \omega_{sQ}(nT_b)\right]\cos(\phi-\hat{\phi}) \end{aligned} \tag{6.13}$$

Equation 6.13 can be simplified by substituting C_I and C_Q with the combinations of the real and imaginary parts of the CSS as defined in Chapter 3. Thus, 6.13 can be written as

$$\begin{aligned} e(nT_b) = &- \frac{1}{2T_b}\int_0^{T_b} 2\left[C_r^2 + C_i^2\right]dt \cdot \sin(\phi-\hat{\phi}) \\ &+ \left[\omega_{cQ}(nT_b) - \omega_{sI}(nT_b)\right]\sin(\phi-\hat{\phi}) \\ &- \left[\omega_{sI}(nT_b) + \omega_{sQ}(nT_b)\right]\cos(\phi-\hat{\phi}) \end{aligned} \tag{6.14}$$

where

$$\begin{aligned} \frac{1}{2T_b}\int_0^{T_b} 2\left[C_r^2 + C_i^2\right] dt &= \frac{2LT_c}{2T_b} \\ &= \frac{2T_b}{2T_b} \\ &= 1 \end{aligned} \tag{6.15}$$

L denotes the spreading sequence length and T_c the chip period of the CSS.

By substituting 6.15 into 6.23, the error signal can be written as

$$\begin{aligned} e(nT_b) = &- \sin(\phi - \hat{\phi}) \\ &+ [\omega_{cQ}(nT_b) - \omega_{sI}(nT_b)]\sin(\phi - \hat{\phi}) \\ &- [\omega_{sI}(nT_b) + \omega_{sQ}(nT_b)]\cos(\phi - \hat{\phi}) \end{aligned} \tag{6.16}$$

where it is assumed that there is zero time shift between the incoming spreading codes and the despreading codes at the receiver. The produced error signal is low-pass filtered and used to control the NCO to recover the quadrature carriers.

It is important to note that the complex despreading codes C_I and C_Q are used in the DD-CCRL to despread the quadrature and in-phase branch, respectively, which is the exact opposite of the despreading and data detection processes. This is to ensure that auto correlation terms will be formed as a result of the product with the DD-CCRL error signal, as shown in 6.13, otherwise a cross correlation term will emerge as a result of the product with the DD-CCRL error signal, which would be very small and would nevertheless lead to insufficient carrier tracking capability.

6.3.2 Dual Channel QPSK Coherent Complex Decision-Directed Costas Carrier Recovery Loop

The block diagram of the coherent complex DD-CCRL used for carrier tracking in the dual channel QPSK DSSS configuration, is depicted in Figure 6.3.

The input of the dual channel QPSK DSSS receiver is given as

$$r(t) = d_1(t)\cdot C_I \cdot \cos(2\pi f_c t + \phi) - d_2(t)\cdot C_Q \cdot sin(2\pi f_c t + \phi) + n(t) \tag{6.17}$$

where all the symbols are as defined in the previous section.

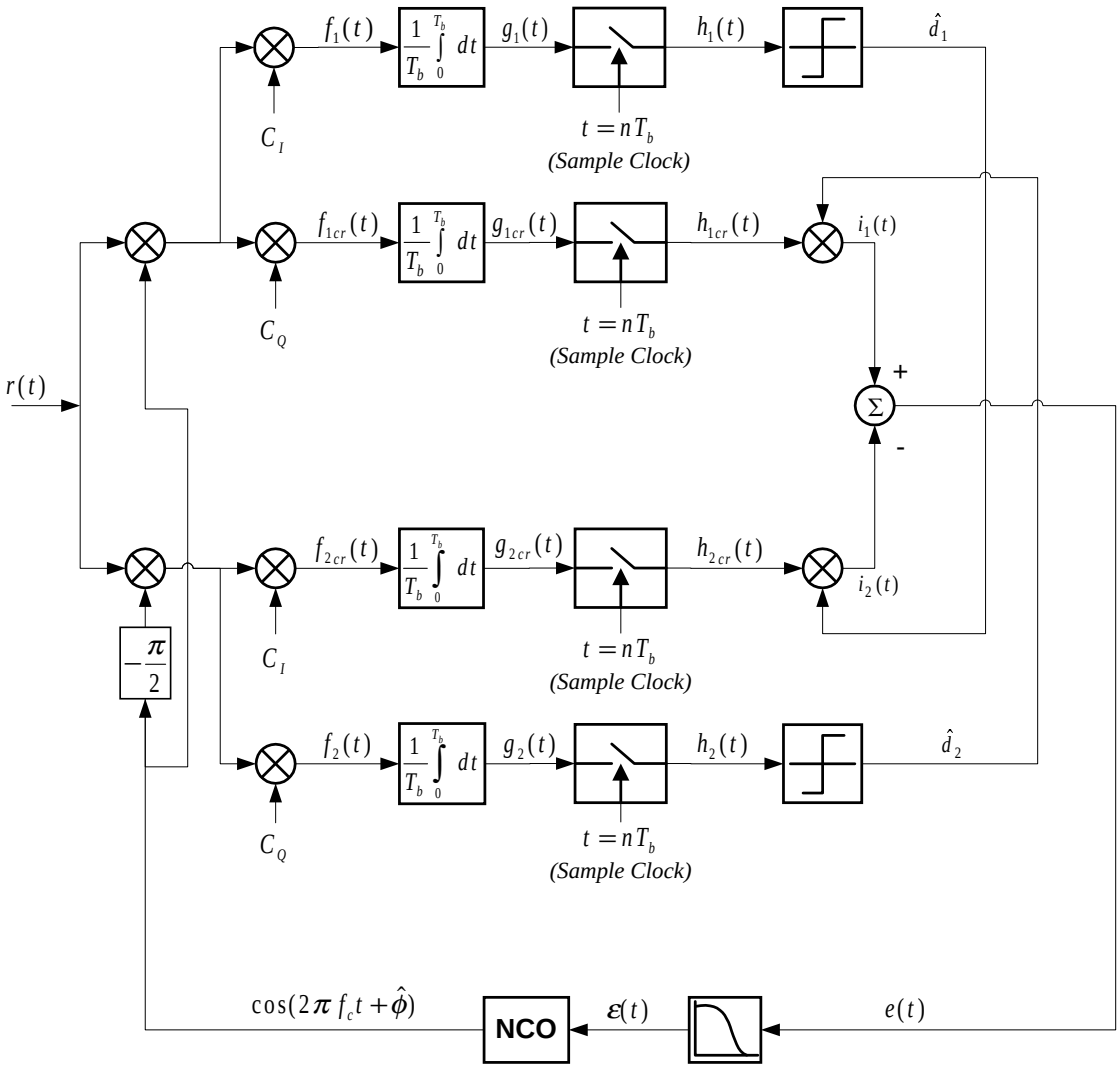

FIGURE 6.3: Block diagram of the dual channel QPSK Complex Decision-Directed Costas Carrier Recovery Loop

Following a similar derivation as that used for the balanced QPSK DSSS system, after elimination of the high frequency components and despreading, the in-phase and quadrature branch signals are integrate-and-dumped to yield $g_1cr(t)$ and $g_2cr(t)$, respectively:

$$\begin{aligned} g_{1cr}(t) &= \frac{d_1(t)\cos(\phi-\hat{\phi})}{2T_b}\int_0^{T_b} C_I C_Q dt \\ &- \frac{d_2(t)\sin(\phi-\hat{\phi})}{2T_b}\int_0^{T_b} C_Q C_Q dt \\ &+ \frac{\cos(\phi-\hat{\phi})}{2T_b}\int_0^{T_b} n_c(t) C_Q dt \\ &- \frac{\sin(\phi-\hat{\phi})}{2T_b}\int_0^{T_b} n_s(t) C_Q dt \end{aligned} \tag{6.18}$$

$$\begin{aligned} g_{2cr}(t) &= \frac{d_1(t)\sin(\phi-\hat{\phi})}{2T_b}\int_0^{T_b} C_I C_I dt \\ &+ \frac{d_2(t)\cos(\phi-\hat{\phi})}{2T_b}\int_0^{T_b} C_I C_Q dt \\ &+ \frac{\sin(\phi-\hat{\phi})}{2T_b}\int_0^{T_b} n_c(t) C_I dt \\ &+ \frac{\cos(\phi-\hat{\phi})}{2T_b}\int_0^{T_b} n_s(t) C_I dt \end{aligned} \tag{6.19}$$

By applying the same definitions used for the balanced QPSK DSSS configuration, equations 6.18 and 6.19 can be written as

$$\begin{aligned} g_{1cr}(t) &= \frac{d_1(t)\cos(\phi-\hat{\phi})}{2T_b}\int_0^{T_b} C_I C_Q dt \\ &- \frac{d_2(t)\sin(\phi-\hat{\phi})}{2T_b}\int_0^{T_b} C_Q C_Q dt \\ &+ \omega_{cQ}(t)\cos(\phi-\hat{\phi}) \\ &- \omega_{sQ}(t)\sin(\phi-\hat{\phi}) \end{aligned} \tag{6.20}$$

and

$$\begin{aligned} g_{2cr}(t) &= \frac{d_1(t)\sin(\phi-\hat{\phi})}{2T_b}\int_0^{T_b} C_I C_I dt \\ &+ \frac{d_2(t)\cos(\phi-\hat{\phi})}{2T_b}\int_0^{T_b} C_I C_Q dt \end{aligned}$$

$$+ \quad \omega_{cI}(t)\sin(\phi-\hat{\phi})$$

$$+ \quad \omega_{sI}(t)\cos(\phi-\hat{\phi}) \tag{6.21}$$

The integrate-and-dump outputs are sample-and-hold at optimum time instants at the end of each integration period (at time instants $t = nT_b$ for $n = 0, 1, 2, ...$).

The sampled in-phase and quadrature branches are cross multiplied by the data decisions, $\hat{d}_2$ and $\hat{d}_1$, made on the quadrature and in-phase branches, respectively, in the despreading and data detection processes, to eliminate the data modulation on the branches. These results are used to form the DD-CCRL error signal by subtracting the quadrature samples from the in-phase samples. This is also based on a decision-directed method and has the advantage of eliminating the additional noise from the tracking loop caused by data modulation. The error signal is given by

$$\begin{aligned} e(nT_b) = & - \frac{1}{2T_b}\int_0^{T_b}[C_I C_I + C_Q C_Q]\,dt \cdot \sin(\phi-\hat{\phi}) \\ & + [\omega_{cQ}(nT_b) - \omega_{sI}(nT_b)]\sin(\phi-\hat{\phi}) \\ & - [\omega_{sI}(nT_b) + \omega_{sQ}(nT_b)]\cos(\phi-\hat{\phi}) \end{aligned} \tag{6.22}$$

which is the same as for the balanced QPSK DSSS system, and 6.22 can in the same manner be simplified to

$$\begin{aligned} e(nT_b) = & - \sin(\phi-\hat{\phi}) \\ & + [\omega_{cQ}(nT_b) - \omega_{sI}(nT_b)]\sin(\phi-\hat{\phi}) \\ & - [\omega_{sI}(nT_b) + \omega_{sQ}(nT_b)]\cos(\phi-\hat{\phi}) \end{aligned} \tag{6.23}$$

where it is assumed that there is zero time shift between the incoming spreading codes and the despreading codes at the receiver. The resultant error signal is low-pass filtered and used to control the NCO to recover the quadrature carriers.

It is also important to note that the composite despreading codes C_I and C_Q are used in the DD-CCRL to despread the quadrature and in-phase branch, respectively, which is exactly opposite to the despreading and data detection processes. The reason for this is to ensure that auto correlation terms will be formed in the product with the DD-CCRL error

signal, as shown in Equation 6.22, otherwise a cross correlation term would be present in the product with the DD-CCRL error signal, resulting in a very small error signal that would jeopardize the carrier tracking process.

6.4 SPREADING CODE SYNCHRONIZATION

The majority of papers on code synchronization loops design for DSSS communication systems concentrate on non-coherent schemes employing binary spreading sequences. These loop structures comprise early and late arm structures with squaring devices which are very prone to arm imbalance effects. In this dissertation a combined coherent carrier recovery and Decision-Directed Delay-Lock-Loop (DD-DLL) synchronization scheme for complex DSSS communication systems are proposed. The novelty of the technique lies in the fact that it extends the structure proposed by de Gaudenzi et al [8] to enable synchronization of systems employing both binary and complex spreading sequences. Typical advantages include features such as less sensitivity to arm imbalance problems due to the elimination of squaring devices, improved tracking capability and simplified hardware by requiring only two correlators in stead of four in the DD-CDLL structure. The simplified loop structures are the direct result of the novel use of unique combinations of the real and imaginary parts of the spreading codes used in both the spreading, demodulation/despreading and code tracking processes and leads to the elimination of unwanted cross product interference terms when employing complex spreading sequences. The loop response is analyzed analytically and its performance verified through computer simulation when employing both binary as well as new families of complex Non-Linearly Interpolated Root-of-Unity (NLI-RU) filtered complex spreading sequences, including a subclass of Analytical Bandlimited Complex (ABC) spreading sequences [4].

6.4.1 Code Acquisition

Prior to acquisition, the unique combinations of complex spreading codes, generated at the transmitter and receiver, are not in synchronism. In order to achieve code locking, a course sliding correlation [38] is first performed on the in-phase and quadrature phase branches. The modulus of these two results are combined and provided as input to a threshold detector.

The outputs of the integrators on the in-phase and quadrature phase branches at the

receiver are given by

$$g_1(t) = \frac{1}{2T_b} d_1(t) \int_0^{T_b} C_I C_I(t - T_d)\, dt + \omega_{c_I}(t) \tag{6.24}$$

and

$$g_2(t) = \frac{1}{2T_b} d_1(t) \int_0^{T_b} C_Q C_Q(t - T_d)\, dt - \omega_{s_Q}(t), \tag{6.25}$$

respectively, as defined in Chapter 5. Assume that there is a time shift $T_d = iT_c$ between the received spreading codes and the local reference spreading codes in the receiver, where $i = 0, 1, 2, \ldots$ and T_c is one chip duration. The signals $g_1(t)$ and $g_2(t)$ are sampled-and-hold and summed. The absolute value of this summed result, illustrated in Figure 6.4, is compared with a predetermined threshold.

The output of the threshold detector controls the clock driving the complex spreading sequence generator. It controls the clock in such a way that when the threshold is not exceeded, the clock is disabled for one clock cycle at the end of the punctual spreading sequence pattern. During the initial synchronization time the coherent DD-CDLL is in an open loop free running mode. Once the threshold is exceeded, the clock is enabled and the coherent DD-CDLL is switched to a closed loop mode. The end result is that the local receiver complex spreading sequence generator will be aligned to within one chip period with the transmitted spreading sequence, yielding *code lock*.

6.4.2 Code Tracking

6.4.2.1 Balanced Complex Decision-Directed Delay-Lock-Loop

Figure 6.5 shows the block diagram for the balanced complex decision-directed DLL synchronization scheme.

The incoming signal $r(t)$ to the coherent CDLL, shown in Figure 6.5, can be modelled as

$$\begin{aligned} r(t) \quad = \quad & \sqrt{P} d(t - T_d) C_I(t - T_d) \cos(2\pi f_c t + \phi) \\ & + \sqrt{P} d(t - T_d) C_Q(t - T_d) \sin(2\pi f_c t + \phi) \\ & + n(t) \end{aligned} \tag{6.26}$$

where P is the average power of the signal, $d(t)$ is the binary data stream, $C_I(t)$ and $C_Q(t)$ is the data-synchronous in phase and quadrature phase combinations of the real and imaginary

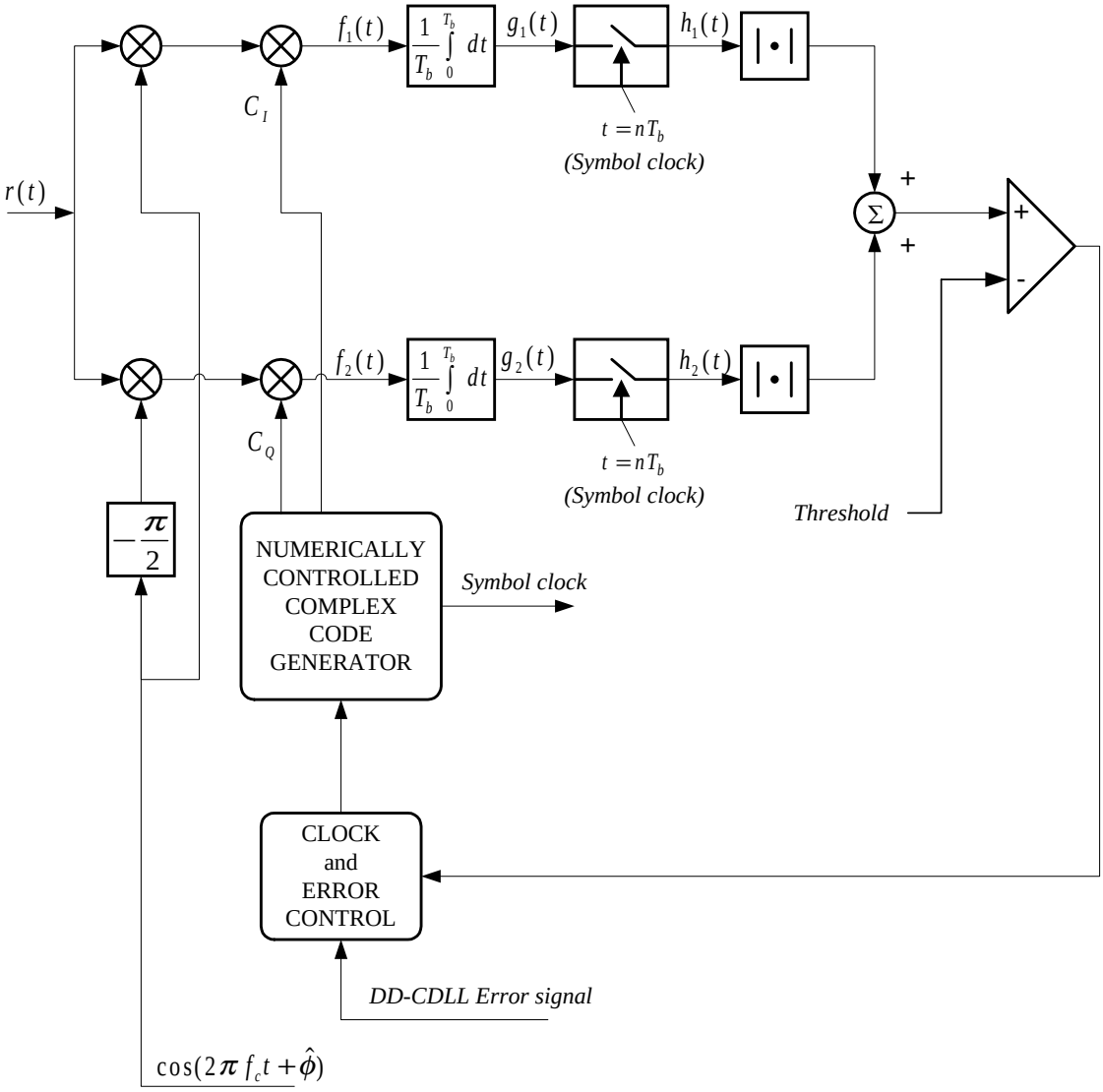

FIGURE 6.4: Block diagram of the acquisition circuitry.

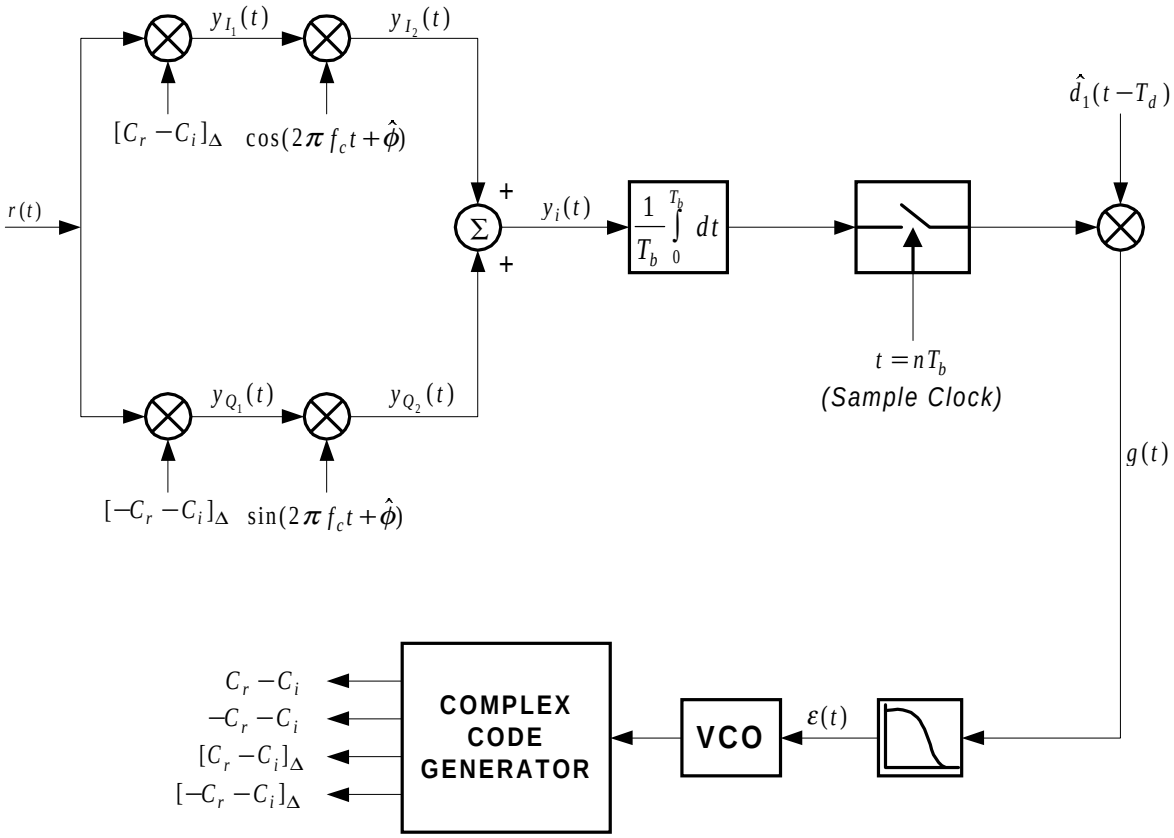

FIGURE 6.5: Block diagram of the Balanced Complex Decision-Directed Delay Lock Loop

parts of complex spreading codes, repectively. T_d is the transmission delay, f_c is the carrier frequency, ϕ is the initial carrier phase and $n(t)$ is **A**dditive **W**hite **G**aussian **N**oise (AWGN) with double-sided power spectral density (PSD) $\frac{N_0}{2}$. We also assume that

$$d(t) = \sum_{i=-\infty}^{\infty} d_i q(t - iT_b) \tag{6.27}$$

where $\{d(t)\}$ are symbols selected from the alphabet $\{-1, +1\}$, and $q(t)$ is the NRZ pulse with bit duration T_b. The spreading codes have a chip duration of T_c seconds.

The code generator produces four sets of spreading code combinations. The first two are variable delay replicas of the combinations used at the transmitter and the second two are composite signals, which can be defined as

$$C_I(t - T_d) = C_r(t - T_d) - C_i(t - T_d) \tag{6.28}$$

and

$$C_Q(t - T_d) = -C_r(t - T_d) - C_i(t - T_d) \tag{6.29}$$

$$\begin{aligned} C_{I\Delta}(t-\hat{T}_d) = [C_r(t - \hat{T}_d - \Delta) - C_i(t - \hat{T}_d - \Delta)] \\ -[C_r(t-\hat{T}_d+\Delta) - C_i(t-\hat{T}_d+\Delta)] \end{aligned} \tag{6.30}$$

and

$$\begin{aligned} C_{Q\Delta}(t - \hat{T}_d) = [-C_r(t-\hat{T}_d-\Delta) - C_i(t-\hat{T}_d-\Delta)] \\ -[-C_r(t-1\hat{T}_d+\Delta) - C_i(t-\hat{T}_d+\Delta)] \end{aligned} \tag{6.31}$$

where Δ is a fixed time shift and $\hat{T}_d$ is the estimated transmission code delay. We can now decompose the AWGN $n(t)$ in Equation (11.1) into its in-phase and quadrature components

$$n(t) = n_c(t)\cos(2\pi f_c t+\phi) - n_s(t)\sin(2\pi f_c t+\phi) \tag{6.32}$$

where $n_c(t)$ and $n_s(t)$ are two mutually independent white Gaussian processes with PSD N_0.

The incoming signal $r(t)$ is divided into an in-phase and quadrature phase branch at the input of the coherent CDLL. Firstly we consider the in-phase branch. At the output of the

first mixer, where the incoming signal is multiplied by $C_{I\Delta}(t-\hat{T}_d)$, we have

$$\begin{aligned} y_{I_1}(t) &= r(t)C_{I\Delta}(t-\hat{T}_d) \\ &= \sqrt{\frac{P}{2}}d(t-T_d)C_I(t-T_d)C_{I\Delta}(t-\hat{T}_d) \\ &\quad \cos(2\pi f_c t+\phi) \\ &+ \sqrt{\frac{P}{2}}d(t-T_d)C_Q(t-T_d)C_{I\Delta}(t-\hat{T}_d) \\ &\quad \sin(2\pi f_c t+\phi)+\omega_{cI\Delta}(t)\cos(2\pi f_c t+\phi) \\ &- \omega_{sI\Delta}(t)\sin(2\pi f_c t+\phi) \end{aligned} \tag{6.33}$$

where

$$\omega_{cI\Delta}(t) = n_c(t)C_{I\Delta}(t-\hat{T}_d) \tag{6.34}$$

and

$$\omega_{sI\Delta}(t) = n_s(t)C_{I\Delta}(t-\hat{T}_d) \tag{6.35}$$

Assume now that the recovered carrier can be represented as

$$c_1(t) = 2\cos(2\pi f_c t+\hat{\phi}) \tag{6.36}$$

where $\hat{\phi}$ is the estimated carrier phase. Thus, at the output of the second mixer we have

$$\begin{aligned} y_{I_2}(t) &= \sqrt{\frac{P}{2}}d(t-T_d)C_I(t-T_d)C_{I\Delta}(t-\hat{T}_d) \\ &\quad [\cos(4\pi f_c t+\phi+\hat{\phi})+\cos(\phi-\hat{\phi})] \\ &+ \sqrt{\frac{P}{2}}d(t-T_d)C_Q(t-T_d)C_{I\Delta}(t-\hat{T}_d) \\ &\quad [\sin(4\pi f_c t+\phi+\hat{\phi})+\sin(\phi-\hat{\phi})] \\ &+ \omega_{cI\Delta}(t)[\cos(4\pi f_c t+\phi+\hat{\phi})+\cos(\phi-\hat{\phi})] \\ &- \omega_{sI\Delta}(t)[\sin(4\pi f_c t+\phi+\hat{\phi}) \\ &+ \sin(\phi-\hat{\phi})] \end{aligned} \tag{6.37}$$

In the same way we can determine the output of the second mixer of the quadrature phase

branch as

$$\begin{aligned} y_{Q_2}(t) &= \sqrt{\frac{P}{2}} d(t-T_d) C_I(t-T_d) C_{Q\Delta}(t-\hat{T}_d) \\ &\quad [\sin(4\pi f_c t + \phi + \hat{\phi}) - \sin(\phi - \hat{\phi})] \\ &+ \sqrt{\frac{P}{2}} d(t-T_d) C_Q(t-T_d) C_{Q\Delta}(t-\hat{T}_d) \\ &\quad [-\cos(4\pi f_c t + \phi + \hat{\phi}) + \cos(\phi - \hat{\phi})] \\ &+ \omega_{cQ\Delta}(t)[\sin(4\pi f_c t + \phi + \hat{\phi}) - \sin(\phi - \hat{\phi})] \\ &- \omega_{sQ\Delta}(t)[-\cos(4\pi f_c t + \phi + \hat{\phi}) \\ &+ \cos(\phi - \hat{\phi})] \end{aligned} \tag{6.38}$$

After summation of these two branches, and the integration over one bit period ($T_b = LT_c$), where L is the complex spreading sequence length, we obtain the following signal

$$\begin{aligned} y_i(t) &= \sqrt{2P}\frac{1}{T_b}\int_0^{Tb} d(t-T_d)\{C_I(t-T_d)C_{I\Delta}(t-\hat{T}_d) \\ &+ C_Q(t-T_d)C_{Q\Delta}(t-\hat{T}_d)\}\cos(\phi-\hat{\phi})dt \\ &+ \sqrt{2P}\frac{1}{T_b}\int_0^{Tb} d(t-T_d)\{C_Q(t-T_d)C_{I\Delta}(t-\hat{T}_d) \\ &- C_I(t-T_d)C_{Q\Delta}(t-\hat{T}_d)\}\sin(\phi-\hat{\phi})dt \\ &+ \frac{1}{T_b}\int_0^{Tb}\{\omega_{cI\Delta}(t)-\omega_{sQ\Delta}(t)\}\cos(\phi-\hat{\phi})dt \\ &- \frac{1}{T_b}\int_0^{Tb}\{\omega_{sI\Delta}(t)+\omega_{cQ\Delta}(t)\}\sin(\phi-\hat{\phi})dt \end{aligned} \tag{6.39}$$

The unique combinations of the real and imaginary parts of the complex spreading sequence, at the transmitter and receiver, as well as the unique structure of the system, are responsible for the required output signal. This output signal is without any cross terms between the real and imaginary parts of the complex spreading sequence, which will induce a lot of code noise into the system.

The following two terms from equation (6.39) can be simplified as follows

$$\begin{aligned} & C_I(t-T_d)C_{I\Delta}(t-\hat{T}_d) + C_Q(t-T_d)C_{Q\Delta}(t-\hat{T}_d) \\ = \; & 2C_r(t-T_d)C_r(t-\hat{T}_d-\Delta) \\ - \; & 2C_r(t-T_d)C_r(t-\hat{T}_d+\Delta) + 2C_i(t-T_d) \\ & C_i(t-\hat{T}_d-\Delta) - 2C_i(t-T_d)C_i(t-\hat{T}_d+\Delta) \end{aligned} \tag{6.40}$$

and by inspection

$$\begin{aligned} & C_Q(t-T_d)C_{I\Delta}(t-\hat{T}_d) \\ & -C_I(t-T_d)C_{Q\Delta}(t-\hat{T}_d) = 0 \end{aligned} \tag{6.41}$$

Using equations (6.40) and (6.41) to replace the terms in equation (6.39), we get

$$\begin{aligned} y_i(t) &= \sqrt{2P}\frac{1}{T_b}\int_0^{Tb} d(t-T_d)[2C_r(t-T_d) \\ &\quad C_r(t-\hat{T}_d-\Delta)-2C_r(t-T_d)C_r(t-\hat{T}_d+\Delta) \\ &+ 2C_i(t-T_d)C_i(t-\hat{T}_d-\Delta)-2C_i(t-T_d) \\ &\quad C_i(t-\hat{T}_d+\Delta)]\cos(\phi-\hat{\phi})dt+\omega_\Delta(t) \end{aligned} \tag{6.42}$$

where

$$\begin{aligned} \omega_\Delta(t) &= \frac{1}{T_b}\int_0^{Tb}\{[\omega_{cI\Delta}(t)-\omega_{sQ\Delta}(t)]\cos(\phi-\hat{\phi}) \\ &- [\omega_{sI\Delta}(t)+\omega_{cQ\Delta}(t)]\sin(\phi-\hat{\phi})\}dt \end{aligned} \tag{6.43}$$

If all the details relative to the data demodulation process which is performed by successive despreading, integrate-and-dump and sample-and-hold operations on the received signal, are skipped $\hat{d}(t-T_d)$ may be assumed as the estimated data stream. By using $\hat{d}(t-T_d)$ we have

$$\begin{aligned} g(t) &= \sum_{i=-\infty}^{\infty}\{\sqrt{2P}\frac{1}{T_b}\int_0^{Tb} d(t-T_d)\hat{d}(t-T_d) \\ &\quad [2C_r(t-T_d)C_r(t-\hat{T}_d-\Delta) \\ &- 2C_r(t-T_d)C_r(t-\hat{T}_d+\Delta) \\ &+ 2C_i(t-T_d)C_i(t-\hat{T}_d-\Delta) \\ &- 2C_i(t-T_d)C_i(t-\hat{T}_d+\Delta)]\cos(\phi-\hat{\phi})dt \\ &+ \omega_\Delta(t)\}h(t-iT_b) \end{aligned} \tag{6.44}$$

To find the final expression of the open-loop error signal $e(t)$ as input signal to the VCO, which drives the complex code generator at the receiver, after the loop filter $f(t)$, we can retain only the DC component of the error signal in equation (6.44) and also neglect the self-noise contribution.

By using $P_e(\varepsilon)$, the BER of the BPSK data demodulator can be determined, when a fixed normalized code timing error ε is present, namely

$$\varepsilon \equiv \frac{T_d-\hat{T}_d}{T_c} \tag{6.45}$$

the DC component can be defined as

$$\begin{aligned} M &= \langle E\{d(t-T_d)\hat{d}(t-T_d)\}\rangle \\ &= 1-2P_e \\ &= 1-2Q[R_c(\varepsilon T_c)\sqrt{\frac{2E_b}{N_0}}\cos(\phi-\hat{\phi})] \end{aligned} \tag{6.46}$$

where

$$Q(x) = \frac{1}{\sqrt{2\pi}}\int_x^{\infty} e^{(\frac{-y^2}{2})}dy \tag{6.47}$$

The normalised auto-correlation peak $R_c(\varepsilon T_c)$ is shown in Figure 6.6. The DC value of $d(t-T_d)\hat{d}(t-T_d)$ would be one in the absence of bit errors. Since the BER is P_e, one regenerated bit every $\frac{1}{P_e}$ bits in $\hat{d}(t)$ will have the incorrect sign. On time averaging the product, $d(t-T_d)\hat{d}(t-T_d)$, the average amplitude is in effect reduced by the amount $2P_e$. Thus $g(t)$ can be written as

$$\begin{aligned} g(t) &= \{\sqrt{2P}\frac{1}{T_b}\int_0^{Tb}(1-P_e)X(t,T_d,\Delta)\cos(\phi-\hat{\phi})dt\} \\ &\quad \otimes f(t) + \omega_{\Delta}(t)\hat{d}(t)\otimes f(t) \end{aligned} \tag{6.48}$$

where

$$\begin{aligned} X(t,T_d,\Delta) &= 2C_r(t-T_d)C_r(t-\hat{T}_d-\Delta) \\ &- 2C_r(t-T_d)C_r(t-\hat{T}_d+\Delta) \\ &+ 2C_i(t-T_d)C_i(t-\hat{T}_d-\Delta) \\ &- 2C_i(t-T_d)C_i(t-\hat{T}_d+\Delta) \end{aligned} \tag{6.49}$$

Define the average autocorrelation function as

$$\begin{aligned} R_c(\tau) &\equiv \frac{1}{NT_c}\int_0^{NT_c} c(t)c(t+\tau)d\tau \\ &= \frac{1}{T_b}\int_0^{T_b} c(t)c(t+\tau)d\tau \end{aligned} \tag{6.50}$$

Thus,

$$\frac{1}{T_b}\int_0^{T_b} X(t,T_d,\Delta)dt = R_c(-\Delta+\varepsilon T_c) - R_c(\Delta+\varepsilon T_c) \tag{6.51}$$

where

$$R_c(-\Delta+\varepsilon T_c) \equiv R_r(-\Delta+\varepsilon T_c) + R_i(-\Delta+\varepsilon T_c) \tag{6.52}$$

and

$$R_c(\Delta+\varepsilon T_c) \equiv R_r(\Delta+\varepsilon T_c) + R_i(\Delta+\varepsilon T_c) \tag{6.53}$$

The final error signal, $e(t)$, is therefore

$$\begin{aligned} e(t) &= \sqrt{2P}(1-P_e)[R_c(-\Delta+\varepsilon T_c)-R_c(\Delta+\varepsilon T_c)] \\ &\quad \cos(\phi-\hat{\phi})\} \otimes f(t)+\omega_\Delta(t)\hat{d}(t)\otimes f(t) \end{aligned} \tag{6.54}$$

The error function $V(\varepsilon)$ can be defined as

$$V(\varepsilon) = R_c(-\Delta+\varepsilon T_c) - R_c(\Delta+\varepsilon T_c) \tag{6.55}$$

and the normalised error function is depicted in Figure 6.7. By defining the following

$$N(t) \equiv \omega_\Delta(t)\hat{d}(t) \tag{6.56}$$

$$\eta \equiv \frac{d}{d\varepsilon}\left[R_c(-\Delta+\varepsilon T_c) - R_c(\Delta+\varepsilon T_c)\right] \mid \varepsilon = 0 \tag{6.57}$$

$$M_0 \equiv M(0) = 1 - 2Q\left[\sqrt{\frac{2E_b}{N_0}}\cos(\phi-\hat{\phi})\right] \tag{6.58}$$

and

$$S(\varepsilon) \equiv \frac{1}{\eta M_0}\left[R_c(-\Delta+\varepsilon T_c) - R_c(\Delta+\varepsilon T_c)\right] M(\varepsilon) \tag{6.59}$$

the error signal $e(t)$ can be written as

$$\begin{aligned} e(t) &= \sqrt{2P}\eta M_0 \cos(\phi - \hat{\phi}) \\ &\quad \left[S(\varepsilon) + \frac{N(t)}{\sqrt{2P}\eta M_0 \cos(\phi - \hat{\phi})} \right] \otimes f(t) \end{aligned} \tag{6.60}$$

The normalised error characteristic (NEC), $S(\varepsilon)$, of the loop is shown in Figure (6.7), for different values of $\frac{E_b}{N_0}$.

The stochastic differential equation which describes the dynamic behaviour is given by

$$\begin{aligned} \frac{d\varepsilon(t)}{dt} &= Ke(t) \\ &= K\sqrt{2P}\eta M_0 \cos(\phi - \hat{\phi}) \\ &\quad \left[S(\varepsilon) + \frac{N(t)}{\sqrt{2P}\eta M_0 \cos(\phi - \hat{\phi})} \right] \otimes f(t) \end{aligned} \tag{6.61}$$

where K denotes the voltage controlled oscillator (VCO) sensitivity. In the following derivations and expressions the assumption is made that the recovered carrier phase error is negligible, i.e. $\phi - \hat{\phi} \approx 0$, and thus $\cos(\phi - \hat{\phi}) \approx 1$.

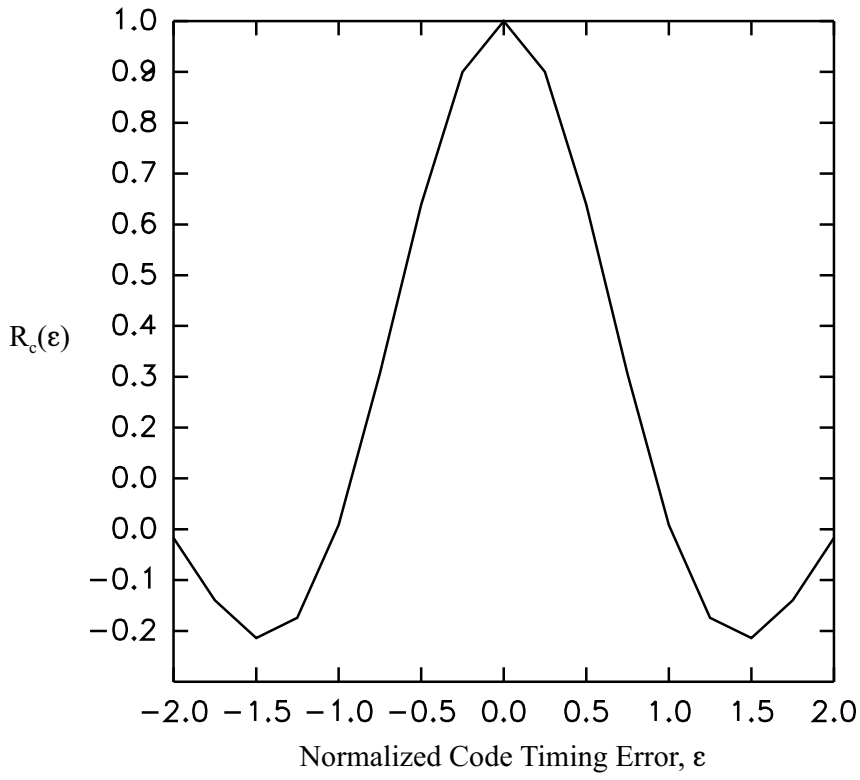

FIGURE 6.6: Normalised autocorrelation peak, $R_c(\varepsilon T_c)$

In the presence of a high signal-to-noise ratio in the loop, $S(\varepsilon)$ can be replaced by its linear equivalent in the neighborhood of $\varepsilon = 0$ and equation (6.61) becomes

$$\begin{aligned} \frac{d\varepsilon(t)}{dt} &= Ke(t) \\ &= K\sqrt{2P}\eta M_0 \cos(\phi - \hat{\phi}) \\ &\quad \left[\varepsilon + \frac{N(t)}{\sqrt{2P}\eta M_0 \cos(\phi - \hat{\phi})}\right] \otimes f(t) \end{aligned} \tag{6.62}$$

The loop transfer function $H(s)$ is defined in [39] as

$$H(s) = \frac{K\sqrt{2P}\eta M_0 F(s)}{s + K\sqrt{2P}\eta M_0 F(s)} \tag{6.63}$$

Assume that a second order passive low pass loop filter of the form

$$F(s) = \frac{s\tau + 1}{s(\tau_1 + \tau_2) + 1)} \tag{6.64}$$

is used. Then the loop transfer function of the tracking loop becomes

$$H(s) = \frac{K\sqrt{2P}\eta M_0 \frac{s\tau_1 + 1}{\tau_1 + \tau_2}}{s^2 + s\frac{1 + K\sqrt{2P}\eta M_0 \tau_2}{\tau_1 + \tau_2} + \frac{1 + K\sqrt{2P}\eta M_0}{\tau_1 + \tau_2}} \tag{6.65}$$

From this expression it can be shown that the natural frequency of the loop, ω_n, is

$$\omega_n = (\frac{K\sqrt{2P}\eta M_0}{\tau_1 + \tau_2})^{\frac{1}{2}} \tag{6.66}$$

and the damping factor, ζ

$$\zeta = \frac{1}{2}(\frac{K\sqrt{2P}\eta M_0}{\tau_1 + \tau_2})^{\frac{1}{2}}(\tau_2 + \frac{1}{K\sqrt{2P}\eta M_0}) \tag{6.67}$$

The same mathematical derivation can be followed for the dual channel QPSK as for the case of the balanced QPSK configuration, as described above. The decision-directed complex delay-locked loop (DD-CDLL) for the dual channel QPSK configuration is depicted in Figure 6.9.

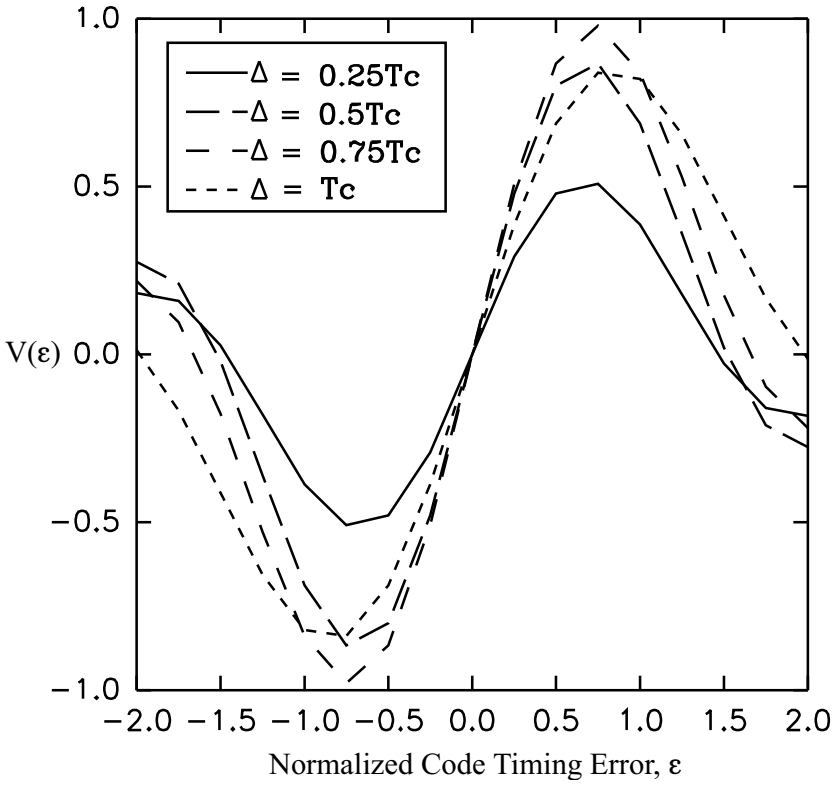

FIGURE 6.7: Normalised error characteristic S-curve for the CDLL

6.5 TIMING RECOVERY

The Decision-Directed Delay-Lock-Loop (DD-DLL) is used, as described in the previous sections, to synchronize the complex spreading sequences, used at the DSSS transmitter and receiver, within one chip period with the accuracy of fractions of a sample. By controlling the global system clock of the receiver by means of the DD-CDLL error signal, code tracking as well as symbol timing are achieved. A complete complex spreading sequence length fits one symbol time period and thus no additional symbol timing recovery is needed.

6.6 CARRIER PHASE AND CODE SYNCHRONISATION: CONCLUSION

Code tracking is performed by means of the coherent Decision-Directed Delay-Lock-Loop (DD-DLL), while the coherent DD-CCRL is responsible for carrier phase tracking. These two synchronisation loops are fully integrated and functions as one combined synchronisation loop. These two interconnected synchronisation loops use mutual synchronisation estimates to perform near optimum carrier phase and code tracking (the

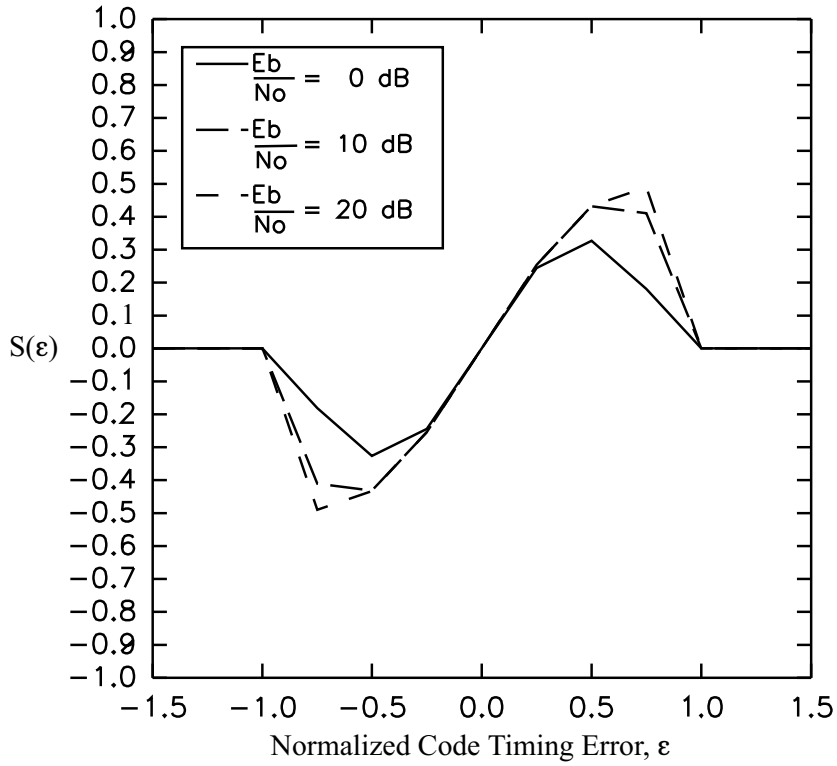

FIGURE 6.8: Normalized error characteristic S-curve for the CDLL for different E_b/N_0 values for $\triangle = 0.75T_c$

optimality of this principle is explained in [21] p.333). The tracking of the carrier phase and the spreading sequence are dependent on each other. This concept is illustrated in Figure 6.10, where the x-axis represents the code timing error in terms of samples, the y-axis represents the carrier phase error and the periodic auto-correlation (PAC) is plotted on the z-axis. A maximum optimum auto-correlation is only obtained with a zero code offset and multiples of 180^o of the carrier phase error. A similar result has been obtained from measurements on the hardware prototype of the DSSS system in Chapter 10 - refer Figures 10.21 and 10.22. It is the function of the combined synchronisation loop to maintain the receiver at this optimum operating point.

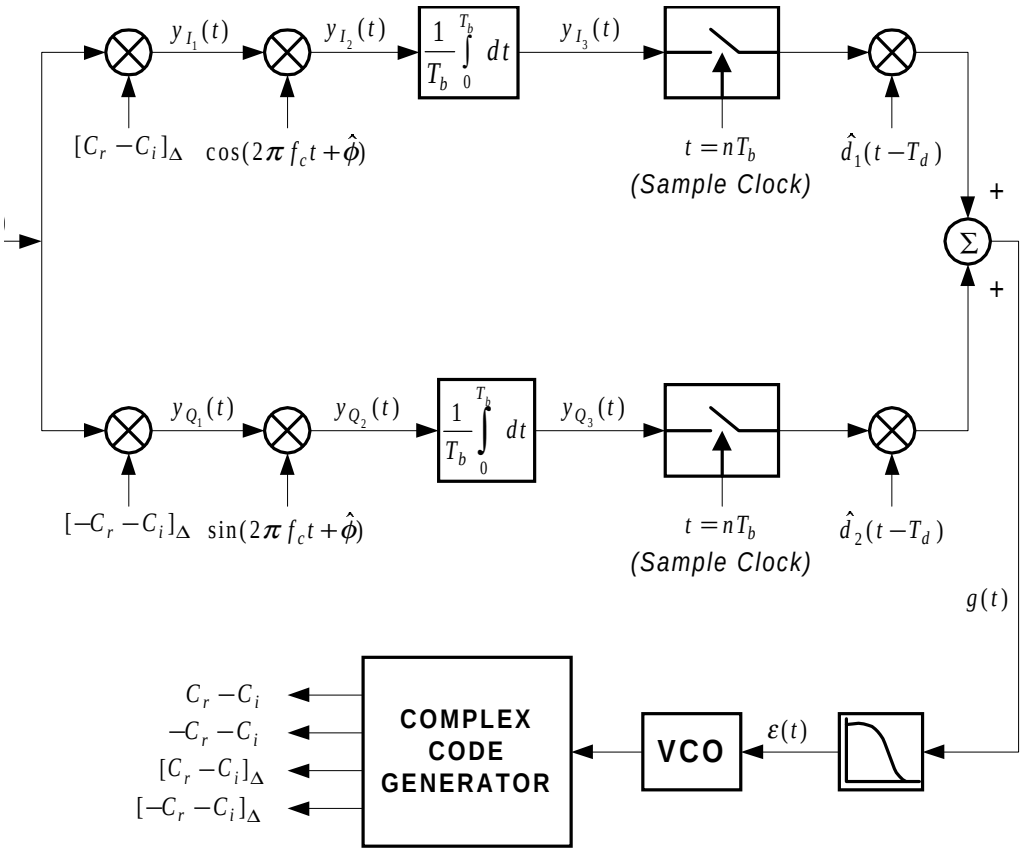

FIGURE 6.9: Block diagram of the Balanced Complex Decision-Directed Delay Lock Loop

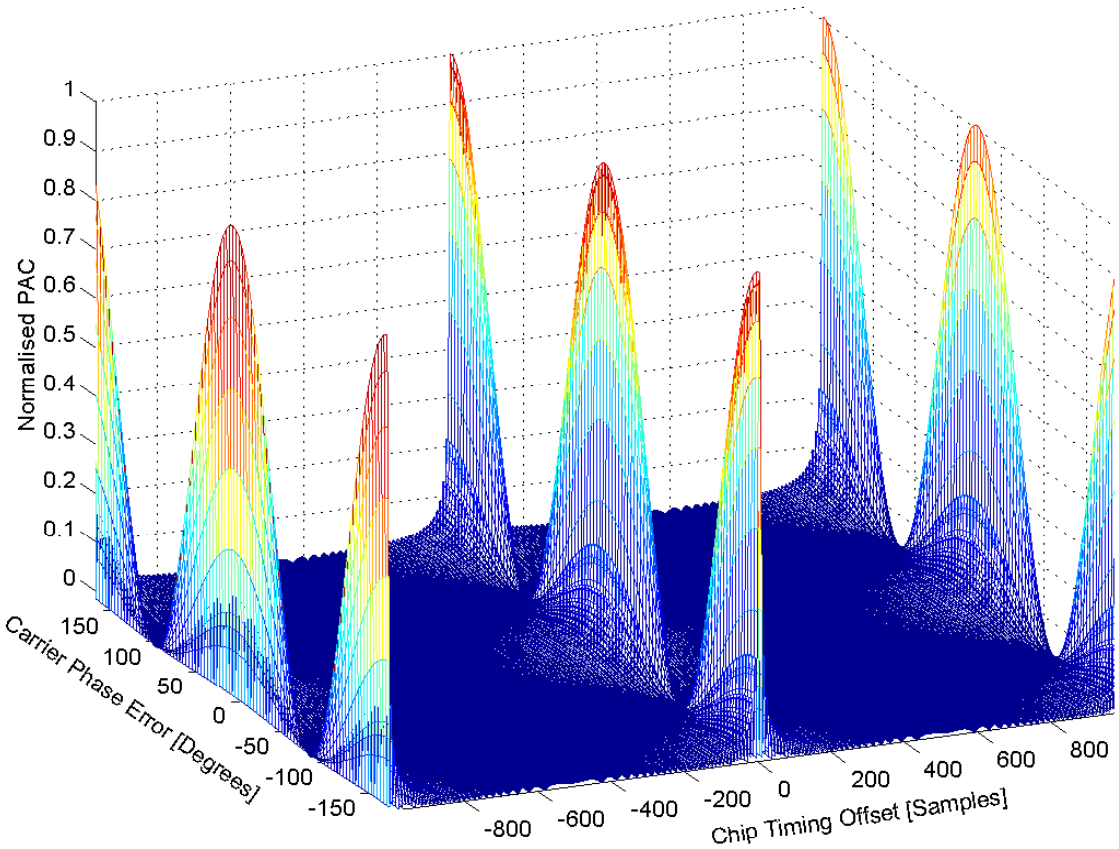

FIGURE 6.10: Illustration of the combination of carrier phase and chip timing synchronisation